# Kelvin–Helmholtz Waves in Precipitating Midlatitude Cyclones

HANNAH C. BARNES

*Pacific Northwest National Laboratory, Richland, Washington*

JOSEPH P. ZAGRODNIK, LYNN A. MCMURDIE, AND ANGELA K. ROWE

*University of Washington, Seattle, Washington*

ROBERT A. HOUZE JR.

*Pacific Northwest National Laboratory, Richland, and University of Washington, Seattle, Washington*

## ABSTRACT

This study examines Kelvin–Helmholtz (KH) waves observed by dual-polarization radar in several precipitating midlatitude cyclones during the Olympic Mountains Experiment (OLYMPEX) field campaign along the windward side of the Olympic Mountains in Washington State and in a strong stationary frontal zone in Iowa during the Iowa Flood Studies (IFloodS) field campaign. While KH waves develop regardless of the presence or absence of mountainous terrain, this study indicates that the large-scale flow can be modified when encountering a mountain range in such a way as to promote development of KH waves on the windward side and to alter their physical structure (i.e., orientation and amplitude). OLYMPEX sampled numerous instances of KH waves in precipitating clouds, and this study examines their effects on microphysical processes above, near, and below the melting layer. The dual-polarization radar data indicate that KH waves above the melting layer promote aggregation. KH waves centered in the melting layer produce the most notable signatures in dual-polarization variables, with the patterns suggesting that the KH waves promote both riming and aggregation. Both above and near the melting layer ice particles show no preferred orientation likely because of tumbling in turbulent air motions. KH waves below the melting layer facilitate the generation of large drops via coalescence and/or vapor deposition, increasing mean drop size and rain rate by only slight amounts in the OLYMPEX storms.

## 1. Introduction

Kelvin–Helmholtz (KH) waves are a form of instability that occurs within a statically stable environment that has strong vertical wind shear. Atmospheric manifestation of this instability was first investigated for its role in clear-air turbulence (e.g., Atlas et al. 1970; Browning and Watkins 1970; Dutton and Panofsky 1970; Browning 1971). Turbulence associated with KH waves has also been suggested to pose an aircraft icing hazard because of its microphysical impact (Pobanz et al. 1994). KH waves have been observed within midlatitude

baroclinic systems in various geographic regions, including off the East Coast of the United States (Wakimoto et al. 1992), the North American Great Plains (e.g., Friedrich et al. 2008; Houser and Bluestein 2011), and mountainous regions in Europe (Houze and Medina 2005) and the United States (e.g., Geerts and Miao 2010; Medina and Houze 2016). A large proportion of these studies observed KH waves within or near the regions of high baroclinicity associated with fronts (Chapman and Browning 1997; Wakimoto et al. 1992; Friedrich et al. 2008; Houser and Bluestein 2011).

Studies, including Geerts and Miao (2010) and Houze and Medina (2005), suggest that mountainous regions are especially conducive to the development of KH waves, since the terrain naturally creates or enhances vertical wind shear in stable flow. KH waves are important because of their transport of heat, momentum, and aerosols (e.g., Browning and Watkins 1970; Gossard et al. 1970;
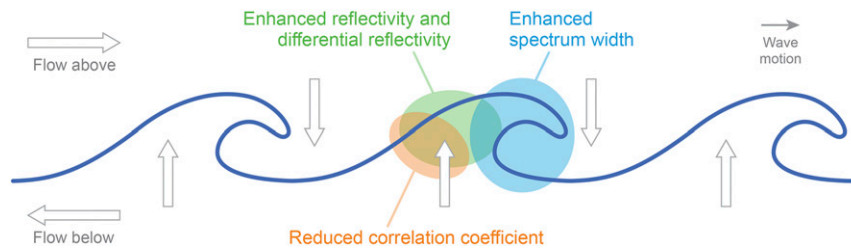
---

FIG. 1. Conceptual model of how KH waves relate to the structure of vertical motion (thick arrows), reflectivity (green), differential reflectivity (green), correlation coefficient (orange), and spectrum width (blue) in an RHI scan. Adapted from Houser and Bluestein (2011).

Browning 1971; Shapiro 1980). Additionally, Houze and Medina (2005) and Houser and Bluestein (2011) found that these waves modify microphysical processes and might even impact the accumulation of precipitation.

Using radar data and in situ aircraft observations, Houze and Medina (2005) showed an example of the upward branch of KH waves increasing supercooled water content and riming above the melting layer when the waves are located near the melting level. Additionally, they provided evidence from aircraft that aggregation is increased by wave-enhanced turbulence. This aggregation in turn further enhances riming and accretion by increasing the size of the collector ice particles. On the basis of these results, Houze and Medina (2005) suggested that KH waves could be an important mechanism responsible for the rapid fallout of precipitation on the windward side of terrain.

Houser and Bluestein (2011) used dual-polarization and dual-Doppler radar analyses of a winter storm in Oklahoma to describe how KH waves impact dual-polarization signatures. Figure 1 is an adaptation of their conceptual model and shows a series of KH waves propagating from left to right. They suggested that KH waves impact the dual-polarization variables most significantly in the upward portion of the waves by altering the microphysical processes acting on the particles and enhancing particle mixing. Specifically, Houser and Bluestein (2011) suggest that riming is induced as the magnitude of the upward motion increases. Additionally, under the right temperature conditions, the ice-multiplication process of Hallett and Mossop (1974) could occur along with the riming. Reflectivity and differential reflectivity are shown to increase in the upward branch of the waves to the extent that these processes produce larger particles (green region in Fig. 1). The supercooled water required for riming may be produced by condensation from the upward motion itself and/or by the vertical advection of liquid water from below the melting level. Houser and Bluestein (2011) further suggest that wave-induced turbulence in the base of the

wave's ridge causes enhanced mixing, which increases particle size and shape diversity. As a result, the average copolar cross-correlation coefficient, which is the correlation of horizontally and vertically polarized radar returns, decreases (orange region in Fig. 1; this variable will subsequently be referred to as the cross-correlation coefficient). Note that the reflectivity and differential reflectivity perturbations extend to greater heights than the correlation coefficient perturbations. Finally, they suggested that turbulence resulting from wave breaking leads to an increase in spectrum width at the crest of the wave (blue region in Fig. 1).

While both Houze and Medina (2005) and Houser and Bluestein (2011) suggest that KH waves have a discernable impact on microphysical processes, both studies had data limitations that prevented further analysis of finer-scale details of the waves and their impacts, including on surface precipitation. In particular, Houze and Medina (2005) lacked ground observations to support their conclusion that KH waves are an important mechanism in the rapid fallout of hydrometeors on the windward side of high terrain. The radar data used by Houser and Bluestein (2011) were too vertically coarse to fully resolve all the possible finescale dual-polarization anomalies associated with the KH waves. It is also important to note that these previous studies analyzed only KH waves occurring near the melting layer, so it remains unknown whether their conclusions pertain to KH waves centered outside of the melting layer. Additionally, state-of-the-art sub-1-km-resolution numerical simulations can explicitly resolve KH waves (Conrick et al. 2018), thus requiring high-quality observations of the waves and coincident microphysical processes and surface precipitation characteristics to compare with the simulations.

Using radar data and ground observations from the Iowa Flood Studies (IFloodS) and the Olympic Mountains Experiment (OLYMPEX), our study analyzes four KH wave events in precipitating midlatitude cyclones to investigate
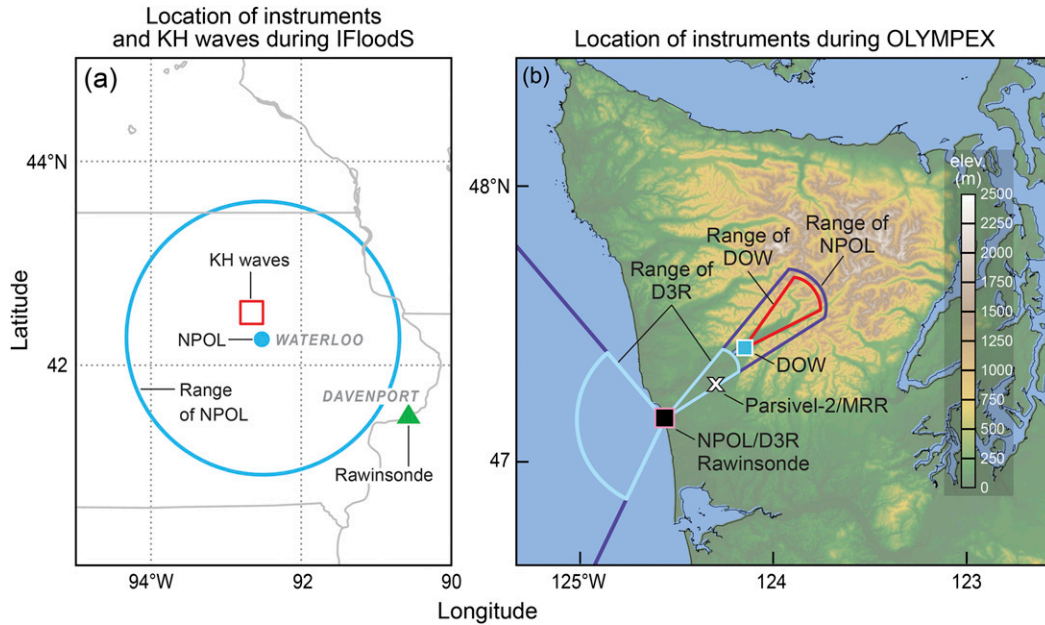
FIG. 2. (a) Map showing the location and range of the NPOL, launch location of rawinsondes, and the approximate location of the KH waves observed on 2 May 2013 during IFloodS. (b) Map showing the location and range of the NPOL, D3R, and DOW radar; the launch location of the rawinsondes; and the location of the ground observations used to study KH waves during OLYMPEX.

1) how KH waves change microphysical processes above, within, and below the melting layer;
2) whether those microphysical changes are significant enough to influence precipitation accumulations at the surface;
3) how terrain impacts KH waves.

## 2. Data and methodology

### a. Field campaigns

The data analyzed in this study were collected during two NASA field campaigns that were designed to validate and improve algorithms used by the Global Precipitation Measurement (GPM) satellite (Skofronick-Jackson et al. 2017; Hou et al. 2014). IFloodS took place in eastern Iowa in May–June 2011, and OLYMPEX took place on the windward side of the Olympic Mountains in Washington State during the 2015/16 winter (Houze et al. 2017). Both field campaigns used collocated instruments (see map in Fig. 2), described below, to describe microphysical processes and their resultant hydrometeor distributions.

### b. Instruments and other data sources

#### 1) RADARS

Radars are one of the most important tools used to observe KH waves. Conventional Doppler radars emit a horizontally oriented pulse and receive the returned power scattered from the population of particles contained within the sample volume. The magnitude of the received power is reported as reflectivity $Z_H$. Reflectivity depends on the concentration, dielectric properties, and the sixth power of the diameter of the hydrometeors. The latter implies that $Z_H$ is most strongly affected by the largest particles sampled by the pulse. Owing to the Doppler effect, these radars also determine the phase shift of the returned power, which is measured and used to derive the mean radial velocity and the width of the velocity spectrum. Radial velocity $V_R$ is the power-weighted average speed at which all targets within the sample volume move toward or away from the radar along the direction of the focused beam. Spectrum width (SW) provides a measure of turbulence and/or shear of the wind component along the beam of the radar.

Dual-polarization Doppler radars emit and receive horizontally and vertically polarized pulses, which allows these radars to determine not only the $Z_H$, $V_R$, and SW, but also several additional variables that describe the size, shape, and orientation of the hydrometeors detected by the radar. Thus, dual-polarization radar data provide insight into the microphysical processes acting on hydrometeors. In this paper we focus on two dual-polarization variables: differential reflectivity $Z_{DR}$ and cross-correlation coefficient $\rho_{HV}$. Differential reflectivity is the ratio of the power return from the

horizontally and vertically oriented pulses and is thus sensitive to geometrical aspects of the particles lying in the beam of the radar. Positive $Z_{DR}$ values indicate oblate targets such as large raindrops or horizontally oriented ice crystals falling with their long axes parallel to Earth's surface. Small or tumbling targets have $Z_{DR}$ values near zero. Because liquid water has a larger dielectric constant than ice, solid ice particles have lower $Z_{DR}$ than water-coated or purely liquid particles, even if the particles are the same size. The cross-correlation coefficient is a measure of the similarity between the horizontally and vertically oriented pulses and is an indication of the diversity in the size, shape, orientation, and water phase of the particles within the radar sample volume. Regions with uniform particle characteristics have $\rho_{HV}$ values near one. At S-band wavelengths, uniform particle populations are associated with $\rho_{HV}$ values near one, while diverse particle populations are typically associated with $\rho_{HV}$ values between 0.95 and 0.85. Note that these $\rho_{HV}$ thresholds slightly vary with wavelength because of resonance effects. For a comprehensive description of dual-polarization radar variables, see Bringi and Chandrasekar (2001).

NASA's dual-polarization S-band radar (NPOL) was deployed during IFloodS and OLYMPEX (Petersen and Krajewski 2018; Petersen et al. 2017). During IFloodS, NPOL was located near Waterloo, Iowa (Fig. 2a; 42.5°N, 92.3°W), and was operated primarily by repeating a sequence of horizontal scans at increasing elevation angles (Petersen and Krajewski 2018), referred to as plan position indicators (PPIs). During OLYMPEX, NPOL was located near Moclips, Washington (Fig. 2b; 47.3°N, 124.2°W) (Petersen and Krajewski 2018). Unlike IFloodS, the NPOL operated primarily in range–height indicator (RHI) mode, with scans changing in elevation at constant azimuth. In this scanning mode, radar data are obtained with the finest possible vertical resolution, which is important for inferring details of microphysical processes and wind shear, both of which vary strongly in the vertical. RHI scans were directed toward the ocean and the mountains.

This study also uses data from three other scanning radars deployed during OLYMPEX [see Houze et al. (2017) for details]. The dual-frequency, dual-polarization Doppler radar (D3R) was collocated with NPOL, operating at Ku and Ka bands with the same scanning sequence as NPOL. Only the Ku band is analyzed in this study. The Center for Severe Weather Research (CSWR) deployed one of its X-band National Science Foundation (NSF)-sponsored Doppler on Wheels (DOW) radars near Amanda Park, Washington (47.5°N, 123.9°W), in the foothills of the Olympic Mountains. The DOW was at an elevation of 72 m and approximately 45 km northeast of NPOL and D3R. This dual-polarization radar

conducted RHI scans up the Quinault Valley and provided data at low levels in the valley below NPOL's beam. The RHI scans conducted by NPOL, D3R, and DOW provide the necessary high-resolution dual-polarization observations of KH waves to address our scientific objectives.

This study uses data from the vertically pointing Micro Rain Radar (MRR) deployed during OLYMPEX. The MRR is a vertically pointing K-band radar that was located at the Fishery site at 47.4°N, 124.0°W, which is approximately 20 km east of the NPOL and D3R radars, and at an elevation of 52 m. The locations of all of these radars are shown in Fig. 2b. MRRs were also deployed during IFloodS but were not in the region where KH waves were observed.

### 2) INSTRUMENTS MEASURING CONDITIONS NEAR THE GROUND

In addition to the radars discussed above, an extensive network of ground observations was deployed during OLYMPEX. In this study data from a Particle Size and Velocity-2 (PARSIVEL-2) disdrometer collocated with the MRR at the Fishery site are used to describe surface drop size characteristics beneath the KH waves. A PARSIVEL-2 disdrometer records the size and fall speed of hydrometeors as they fall through a laser beam. The particles are then separated into 32 separate size and velocity bins that are used to characterize the drop size distribution (DSD) of the precipitation in terms of its mass-weighted mean diameter and droplet concentration. This instrument also provides rain rate calculated from the DSD measurements. PARSIVEL-2 data in this study have a time resolution of 30 s. The PARSIVEL-2 data are part of the dataset described in Petersen and Krajewski (2018). PARSIVEL-2 disdrometers were also deployed during IFloodS but were not situated where the KH waves occurred.

### 3) RAWINSONDES, SATELLITE DATA, AND NUMERICAL MODEL OUTPUT

Rawinsonde data are used during each KH wave event to assess the vertical profile of static stability and vertical wind shear. During IFloodS the nearest rawinsonde station was in Davenport, Iowa, approximately 180 km southeast of the IFloodS NPOL location (University of Wyoming 2013). Despite the spatial separation between the rawinsonde and KH waves, these data are expected to be generally representative of the conditions associated with the KH waves and the impact of this separation is discussed in section 3. During OLYMPEX, rawinsondes were launched from the NPOL site and dropsondes were released over the ocean from the DC-8 aircraft during precipitating events of interest (Petersen and Krajewski 2018).

TABLE 1. Description of the time, duration, location, data available, and frontal features associated with each KH wave event.

| Start date | Start time (UTC) | Duration (h) | Location | Elevation (km) | Location relative to bright band | Front |
|---|---|---|---|---|---|---|
| 2 May 2013 | 1230 | <1 | Iowa | 1–3 | Within | Stationary |
| 9 Dec 2015 | 0700 | <1 | Washington coast | 4–6 | Above | Nonfrontal |
| 12 Dec 2015 | 2030 | ~1 | Quinault Valley | 1–3 | Within | Occluded |
| 17 Dec 2015 | 1200 | 6 | Pacific Ocean, Washington coast, Quinault Valley | 0–2 | Below | Occluded |

Geostationary infrared brightness temperatures from GOES-West and data from the National Centers for Environmental Prediction (NCEP) North American Regional Reanalysis (NARR) are used to describe the large-scale conditions associated with both the IFloodS and OLYMPEX events (Mesinger et al. 2006). These data are produced by NOAA/OAR/ESRL PSD (2004).

## 3. Large-scale conditions in which KH waves occurred

The KH wave events from IFloodS and OLYMPEX analyzed in this study are listed in Table 1. To the authors' knowledge, KH waves were observed only once during IFloodS, on 2 May 2013. However, the authors' commonly observed KH during OLYMPEX. Three OLYMPEX cases included in this study were chosen because of the duration, data quality, and altitude variability of the observed KH waves.

The synoptic conditions associated with the four KH wave cases analyzed in this study are depicted in Fig. 3. The soundings launched at NPOL (for OLYMPEX) and at Davenport (for IFloodS) nearest to the time of the KH waves are shown in Fig. 4. The Richardson number (Ri) is the most commonly used metric to assess whether an environment is conducive to KH waves. It is the ratio of the atmospheric stability to vertical wind shear in a layer. KH waves can develop in an environment with Ri < 0.25 (Miles and Howard 1964) and can be sustained as long as Ri < 1 (Weckwerth and Wakimoto 1992). The bulk Richardson number over a layer is defined as

$$\mathrm{Ri}_b = \frac{N_d^2}{\left(\frac{\partial \mathbf{u}}{\partial z}\right)^2},$$

where $N_d$ is the dry Brunt–Väisälä frequency. A profile of the bulk Ri calculated over 0.25-km intervals during the time of the KH waves is shown in Fig. 5.

During the IFloodS case on 2 May 2013, a meridionally stretched 500-hPa trough was situated east of the Rocky Mountains and an elongated band of clouds was located over Iowa and Minnesota (Fig. 3a). These clouds coincided with a stationary front that was marked by a sharp thermal gradient and a 180° wind shift at 925 hPa (Fig. 3b). Data presented in Figs. 4a and 5a suggest that a strong low-level stable frontal inversion of over 8°C and strong directional shear below 1 km resulted in conditions that could support the development and maintenance of KH waves because the Ri was less than 0.25 in multiple layers below 1 km near Davenport. The radar-observed KH waves were located near Waterloo, which is approximately 180 km to the northwest. Given that the frontal boundary sloped westward with height (not shown), the conditions that supported the development of the radar-observed KH waves likely occurred at somewhat higher altitudes. Commercial aircraft observations (not pictured) near Des Moines, Iowa, showed the shear boundary closer to 2 km at the time of the KH waves. These large-scale conditions on 2 May 2013 were similar to the Oklahoma case analyzed by Houser and Bluestein (2011), which also was a snow event. The National Weather Service noted that this was an unusually strong front (http://www.weather.gov/dmx/maysnow).

On 9 December 2015, during the first OLYMPEX case analyzed in this study, a strong west-southwesterly flow at 500 hPa was impinging on the Washington and Oregon coasts and contained several embedded shortwaves (Figs. 3b,f). One of these shortwaves was associated with a large southwest–northeast-oriented band of clouds passing directly over the Olympic Peninsula at the time of the KH wave observations (Fig. 3b). The atmosphere had moist neutral stability from the surface to 550 hPa (Fig. 4b). These conditions are consistent with the frontal system being of the "atmospheric river" type (Newell et al. 1992; Zhu and Newell 1994, 1998; Ralph et al. 2004; Warner et al. 2012). The KH waves occurred between 4 and 6 km, which is the upper boundary of this moist layer. The drier layers above 6 km were associated with considerably stronger winds from an upper-level jet. The analysis presented in Fig. 5b indicates that multiple layers between 5 and 7 km had Ri values less than 0.25, consistent with the development of KH waves in this layer. However, note that because of the strong winds, the balloon of the 9 December 2015
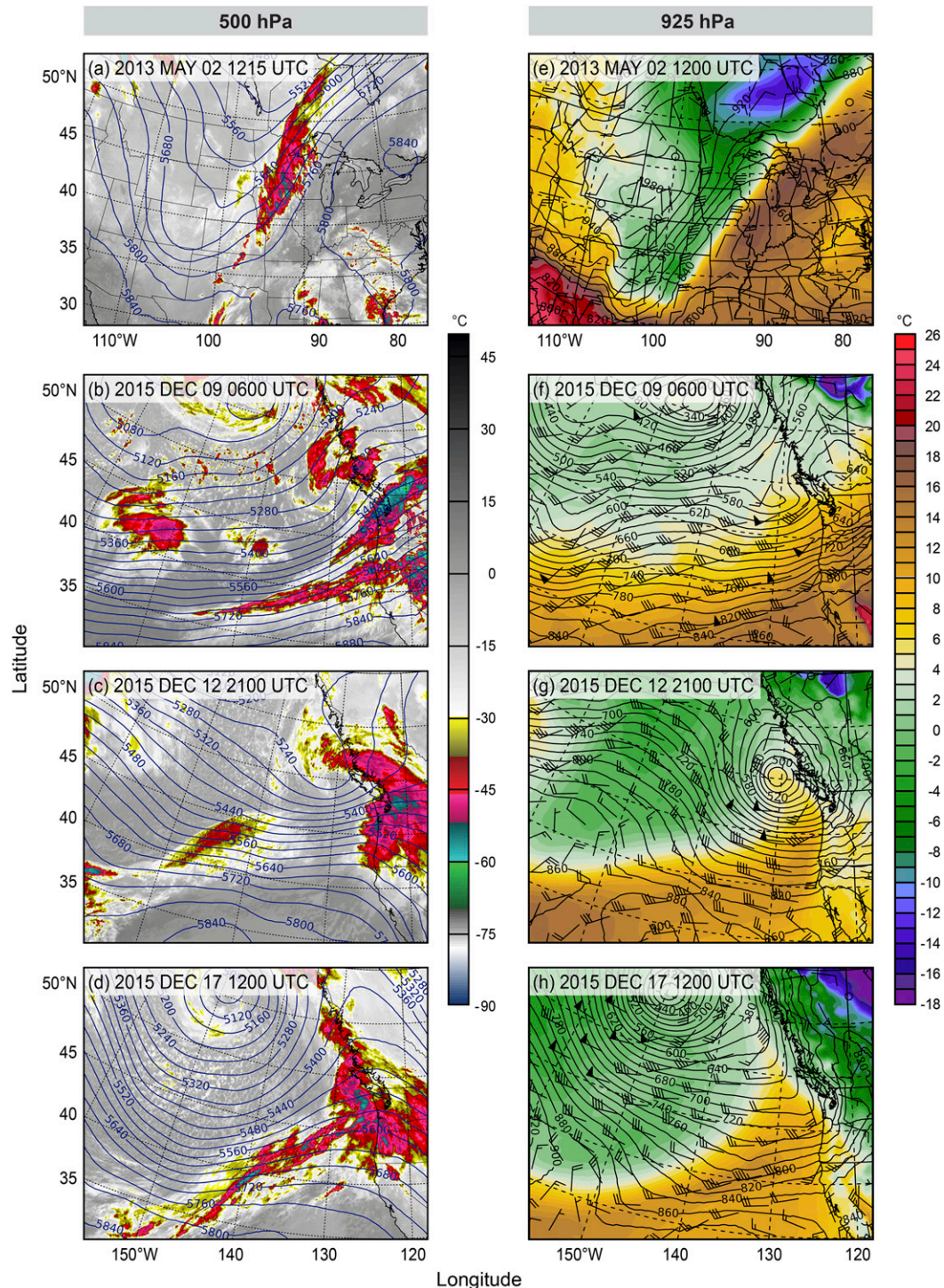
FIG. 3. (left) Infrared brightness temperatures (shading; °C) and 500-hPa heights (contours; m) from NARR at (a) 1215 UTC 2 May 2013, (b) 0600 UTC 9 Dec 2015, (c) 2100 UTC 12 Dec 2015, and (d) 1200 UTC 17 Dec 2015. (right) The 925-hPa temperatures (shading; °C), heights (contours; m), and winds (barbs) from NARR at (e) 1200 UTC 2 May 2013, (f) 0600 UTC 9 Dec 2015, (g) 2100 UTC 12 Dec 2015, and (h) 1200 UTC 17 Dec 2015.
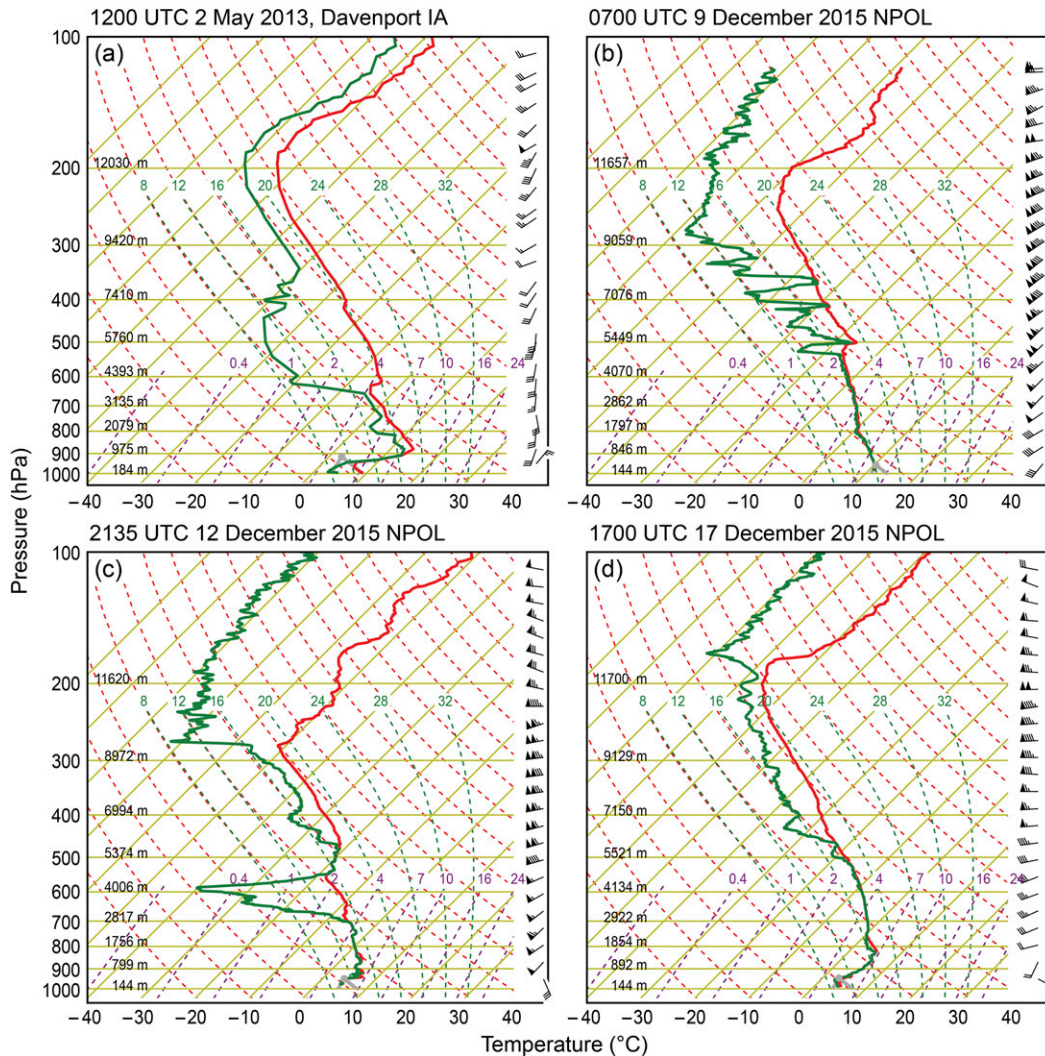
FIG. 4. Rawinsonde data plotted on a skew $T$–log$p$ diagram at (a) 1200 UTC 2 May 2013 in Davenport, (b) 0700 UTC 9 Dec 2015 at NPOL during OLYMPEX, (c) 2135 UTC 12 Dec 2015 at NPOL, and (d) 1700 UTC 17 Dec 2015 at NPOL. In each panel, temperature is the red contour and dewpoint temperature is the green contour. Winds are represented as barbs along the right side of each panel.

sounding was carried far downwind and may not be entirely representative of the conditions where the waves were observed.

An amplifying shortwave trough approached the Olympic Peninsula on 12 December 2015 (Fig. 3c). Associated with this trough was a deep 925-hPa low pressure center positioned off the coast of Vancouver Island (Fig. 3g) and an occluded front extended southward along the coast. The Pacific Northwest was under the broad cloud shield associated with the front (Fig. 3c). In Fig. 4c it can be seen that the front was associated with a small sheared, stable layer near 925 hPa. This layer contained the observed KH waves, and is shown in Fig. 5c to have Ri values less than

one everywhere below 1 km and less than 0.25 between 0.75 and 1 km.

Four soundings from the December 12 case are pictured in Fig. 6: a prefrontal and frontal dropsonde released over the ocean 150 and 195 km west-southwest of NPOL, respectively, plus a prefrontal and frontal radiosonde launched at NPOL. The dropsondes were chosen from a series of nine dropsondes released during two flight legs flown perpendicular to the frontal boundary. The Ri < 0.25 threshold for KH instability (Fig. 6f) was reached below 1.0 km in the frontal ocean sounding and in both coastal soundings. Thus, the large-scale conditions were conducive to KH waves along the coast during the prefrontal and frontal periods and
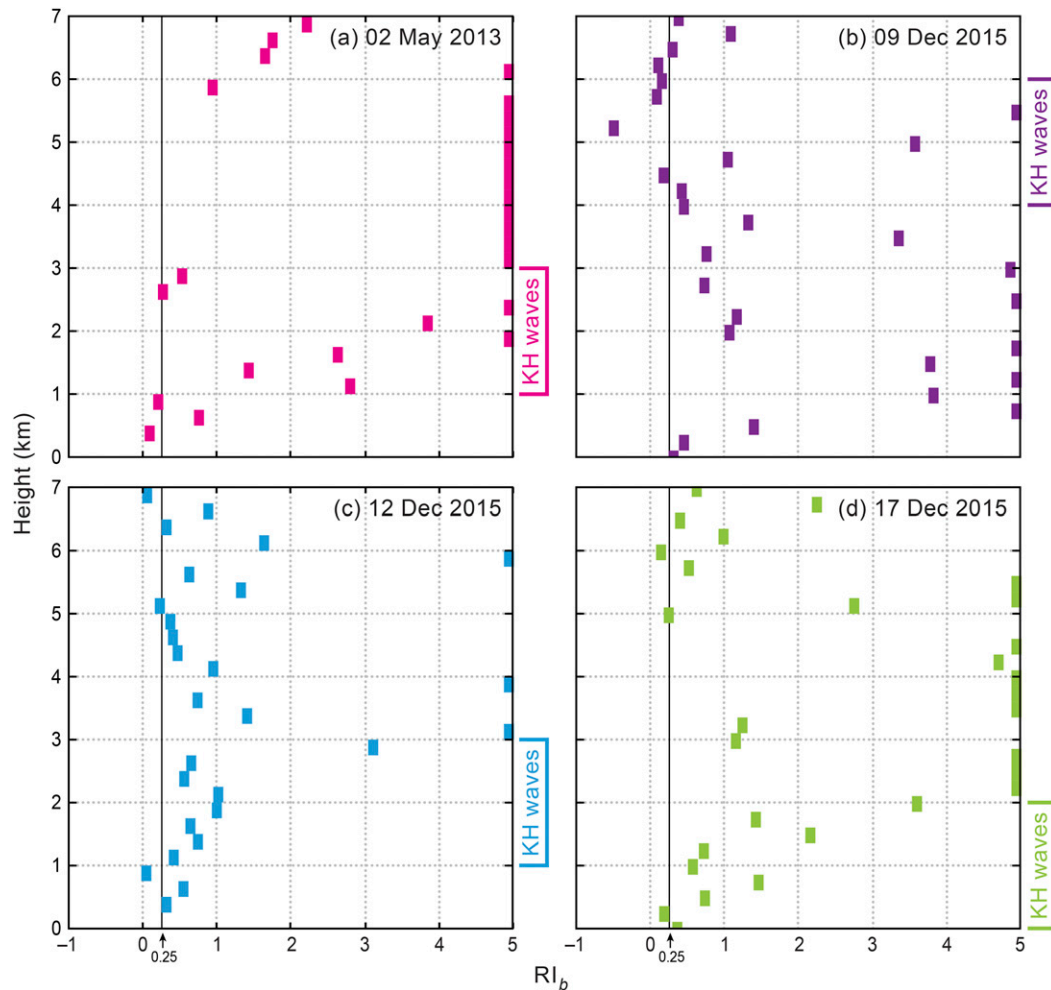
FIG. 5. Vertical profiles of the bulk Richardson number calculated over 0.25-km intervals. Each panel represents a profile from a different sounding: (a) 1200 UTC 2 May 2013 in Davenport, (b) 0700 UTC 9 Dec 2015 at NPOL, (c) 2135 UTC 12 Dec 2015 at NPOL, and (d) 1700 UTC 17 Dec 2015 at NPOL.

away from the influence of topography offshore during the frontal period. However, KH waves were exclusively observed along the coast during the passage of the front, meaning that the KH waves required an additional increase in shear and/or stability beyond these preexisting favorable conditions. The winds in the lowest 0.5 km near the coast (Figs. 6b,c) were modified by topography, as they have both reduced velocity and an increased easterly component compared to the offshore dropsondes. The increase in low-level temperature (Fig. 6a) associated with the approaching front was also suppressed near the coast, resulting in a significant increase in static stability below 0.5 km compared to the frontal offshore sounding. The increased low-level shear and stability near land (Figs. 6d,e) may have resulted from a combination of surface friction and/or blocking of the larger-scale southerly flow (Fig. 3g) by the

Olympic Mountains barrier. Thus, we suggest that the development of KH waves in this event was facilitated by the topography. Conrick et al. (2018) found that removing the Olympic Mountains topography prevented KH waves from forming in this case, further supporting the idea that the low-level shear and stability associated with the occluded front were enhanced by the mountains.

The Olympic Peninsula was beneath the expansive cloud shield of another occluded front on 17 December 2015 (Fig. 3d). However, unlike 12 December 2015, this occluded front was associated with a deep, closed low pressure center in the Gulf of Alaska at 60°N, 150°W. Additionally, the 17 December 2015 occluded front was more well defined, since it had a stronger 925 hPa trough (Figs. 3d,h) and a deeper stable layer (Figs. 4c,d). While the winds veered with height from
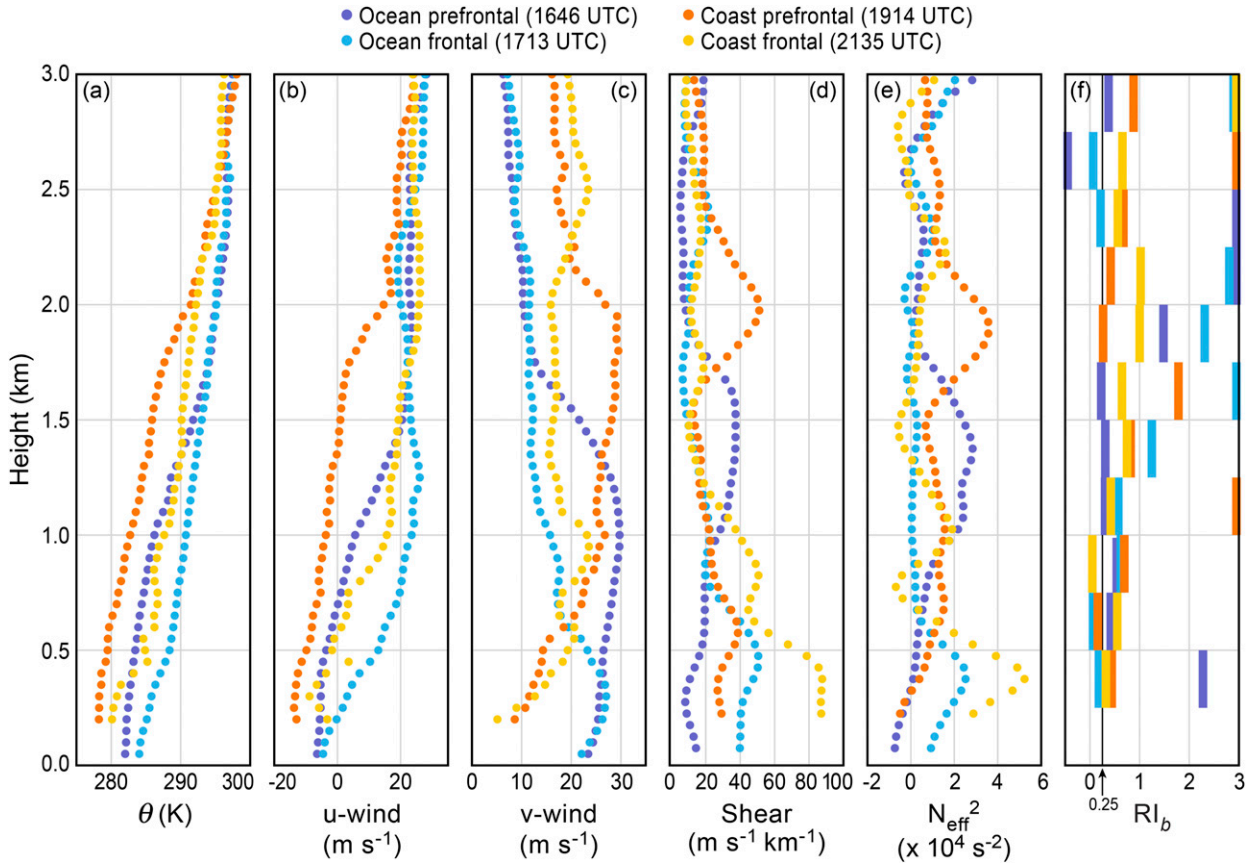
FIG. 6. Vertical profiles of (a) potential temperature (K), (b) zonal winds (m s$^{-1}$), (c) meridional winds (m s$^{-1}$), (d) vertical wind shear (m s$^{-1}$ km$^{-1}$), (e) effective stability scaled by $10^4$ (s$^{-2}$), and bulk Richardson number calculated as in Fig. 5. Profiles from a different OLYMPEX sounding or dropsonde on 12 Dec 2015 are shown: 1646 UTC (46.9°N, 126.1°W) offshore (light blue), 1713 UTC offshore (46.6°N, 126.5°W) offshore (dark blue), 1914 UTC at NPOL (light orange), and 2135 UTC at NPOL (dark orange).

southeasterly to westerly across the stable layer on 17 December 2015, the wind speeds did not vary significantly with height. This strong directional vertical wind shear resulted in the Ri dropping below 0.25 below 1 km (Fig. 5d), which coincides with the central axis of the KH waves on this day.

Comparing the synoptic conditions for these events provides insights into the large-scale environments that support KH waves and how their development may be impacted by mountainous terrain. On 2 May 2013, 12 December 2015, and 17 December 2015, KH waves occurred in association with a near-surface, stable frontal layer, but these KH waves were not unique to one type of front. The presence of KH waves in various types of fronts has also been found by Chapman and Browning (1997), Wakimoto et al. (1992), Friedrich et al. (2008), and Houser and Bluestein (2011). The analysis presented in Fig. 7 compares the zonal and meridional wind, vertical wind shear, and effective static

stability ($N_m^2$ if RH > 90%, $N_d^2$ otherwise) for each case using their respective sounding data. During the cases associated with near-surface fronts, the low-level vertical wind shear reaches values greater than 50 m s$^{-1}$ km$^{-1}$ and the effective static stability peaks above 4 s$^{-2}$ in the lowest 1 km. The maximum magnitude of the vertical wind shear is relatively similar in each of the three frontal cases. However, the magnitude of the effective static stability is much higher during the IFloodS case than during any of the OLYMPEX cases. Additionally, it is notable that the IFloodS case occurred along an anomalously strong front, while the frontal boundaries associated with the OLYMPEX cases had weak temperature gradients, typical of fronts impacting the Olympic Mountains. In fact, these three OLYMPEX cases are just a subset of all the KH wave events observed during OLYMPEX. Observations of KH waves during OLYMPEX were common, which suggests that the terrain may enhance the vertical shear and thus enable KH
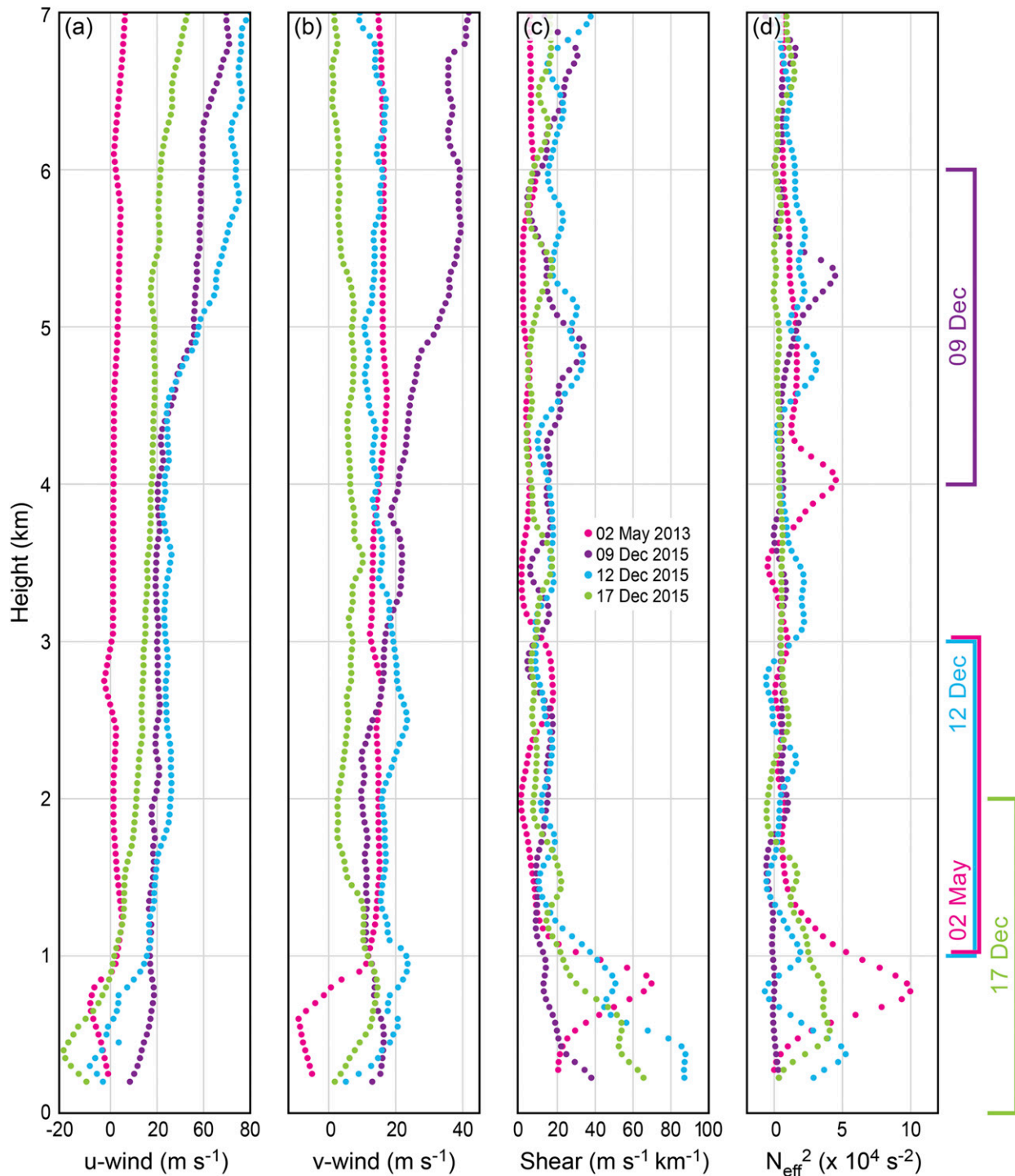
FIG. 7. Vertical profiles of (a) zonal winds (m s$^{-1}$), (b) meridional winds (m s$^{-1}$), (c) vertical wind shear (m s$^{-1}$ km$^{-1}$), and (d) effective stability (s$^{-2}$, scaled by 10$^{4}$). The colors represent profiles calculated by different soundings as in Fig. 5.

waves to develop more easily (Houze and Medina 2005; Medina et al. 2005, 2007). The 9 December case was unique, since the KH waves were not directly associated with a frontal zone but instead formed in the warm sector of a midlatitude cyclone. The KH waves in this case formed along the upper boundary of the deep moist layer, where stability abruptly increased and strong vertical wind shear existed.

## 4. KH waves as seen in PPI scans

Houser and Bluestein (2011) and Medina and Houze (2016) have demonstrated that KH waves can be observed in PPI data as oscillatory patterns in $V_R$, $Z_H$, SW, $Z_{DR}$, and $\rho_{HV}$. The 3.5°-elevation PPI scan from NPOL at 1251 UTC 2 May 2013 over Iowa is shown in Figs. 8a–d. Oscillatory patterns are evident in $V_R$, $Z_{DR}$, SW, and $\rho_{HV}$ at 42.3°N, 92.8°W. Similar patterns were observed in the 5.4° and 7.4° PPI scans, suggesting that the waves were centered at approximately 2 km above the surface. Images of the NPOL data extending to farther range (not shown) reveal that these waves were located within the brightband layer (the layer of enhanced $Z_H$ associated with melting ice particles). Figure 4a indicates that the 0°C level was near 3 km in Davenport. However, the melting layer is likely lower at the NPOL site, which was in the colder air behind the stationary front (Figs. 3a,e). Similar oscillatory patterns were observed over a period of 30 min.

The 0.5°-elevation PPI scan from D3R's Ku band during the OLYMPEX case at 1454 UTC 17 December 2015 is shown in Figs. 8e–h. The diagonal black line in Figs. 8e–h represents the Washington coastline. D3R captured an extensive region of oscillating $V_R$ and SW near 47.25°N (Figs. 8f,g). While the $V_R$ oscillations on 17 December 2015 (Fig. 8f) do not have the classic oscillatory patterns discussed in Houser and Bluestein (2011) and seen in the IFloodS case discussed above, alternating bands of high and low $V_R$ are clear. The oscillations associated with the KH waves are most apparent in SW (Fig. 8g). Similar oscillations were also observed in the 1.5°-elevation scan for nearly 6 h. Figure 4d shows the KH waves were located at 1-km altitude, which was approximately 1 km below the melting level.

KH waves existed both over land (right of diagonal line) and over the ocean (left of diagonal line), and there is evidence that the steep topography impacted the orientation of KH waves. The orientation of the crests of the waves is different over the ocean than over the rising terrain on the windward side of the mountains (most clearly seen in Fig. 8g). Houze and Medina (2005) suggests the terrain-induced vertical wind shear may modify the orientation of the KH waves by changing the wind shear vector direction. Thus, the Olympic Mountains may be impacting the orientation waves on 17 December 2015 by deflecting the low-level flow to a more easterly direction than is present over ocean.

Even though the KH waves were characterized by distinct oscillations in $V_R$ and SW, an analysis of Fig. 8 suggests that these waves do not always create perturbations in the dual-polarization variables. A close inspection of Fig. 8e within 15 km of the radar indicates that a few weak bands of increased $Z_H$ were observed with the waves. However, $\rho_{HV}$ is unperturbed by the waves (Fig. 8h), likely because it measures the diversity of the hydrometeor types within a radar sample volume, and these waves occurred below the melting level and likely contained only raindrops. The next section uses RHI radar data and ground observations to further explore the degree to which the KH waves impacted microphysical processes and precipitation accumulations.

## 5. Microphysical impact of KH waves

The high-resolution RHI scans from NPOL, DOW, and D3R obtained during OLYMPEX allowed this study to assess how KH waves impact microphysical processes above, within, and below the melting layer, both upstream of and over the terrain. Additionally, ground observations were able to document oscillations in drop size, rain rate, and fall speed for one of the OLYMPEX KH events examined here. Together, these radar and ground data allow us to verify the conceptual model proposed by Houser and Bluestein (2011) and to explore whether these waves significantly impact precipitation accumulations.

### a. RHI scans when KH waves are above the melting layer

Petre and Verlinde (2004), Browning et al. (2012), and Medina and Houze (2015) show that the KH waves can be identified as "breaking wave" and "braided'" structures in SW. An RHI scan at a 56° azimuth angle directed toward the land from D3R's Ku band is shown in Fig. 9. A breaking wave structure is evident in Fig. 9c, where thin filaments of high SW slope upward from left to right between altitudes of 4 and 6 km. Within each vertical column, SW was highest along the central axis of the wave. The black dots in Fig. 9 mark these locations of column maximum SW and thus trace the central location of the wave.

The analysis presented in Fig. 9b shows that the winds had a component directed away from the radar throughout the low to midtroposphere but that their magnitude increased by nearly $20\,\mathrm{m\,s^{-1}}$ between altitudes of 2 and 6 km. These $V_R$ values are consistent with rawinsonde data presented in Fig. 4b, since the RHI shown is oriented nearly parallel to the wind. The $V_R$ data in Fig. 9b also indicate that $V_R$ maximized in excess of $40\,\mathrm{m\,s^{-1}}$ in a thin band just above the crest of the waves. Simpson (1969) and Wakimoto et al. (1992) also found that $V_R$ maximizes just above the crest of KH waves.

The microphysical impacts of KH waves are inferred using dual-polarization variables. The most striking feature in Fig. 9 is the bright band, which is a relatively narrow region of reduced $\rho_{HV}$, enhanced $Z_H$, and
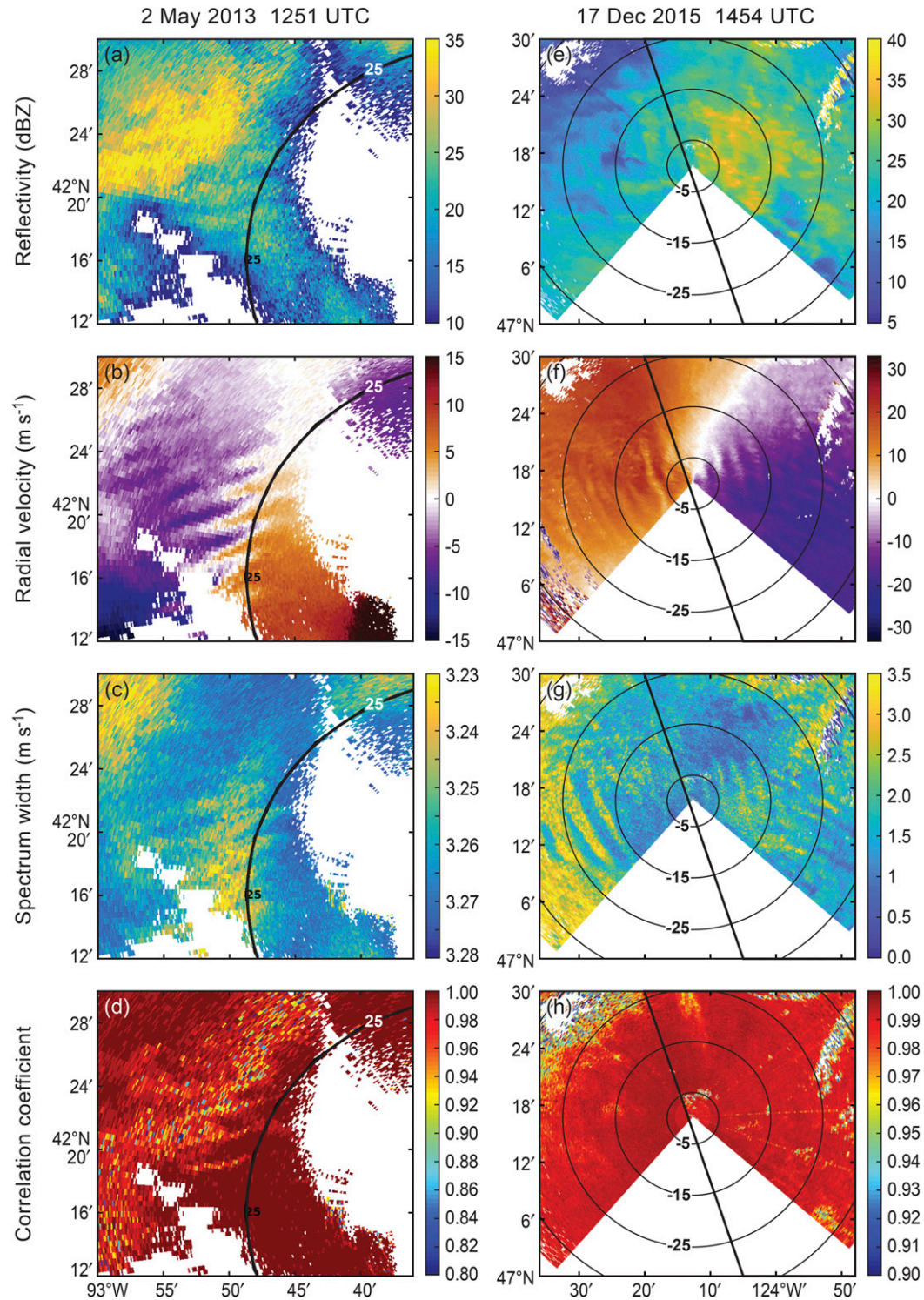
FIG. 8. (left) Radar variables from the 3.5° PPI scan from the NPOL located near Waterloo at 2151 UTC 2 May 2013: (a) reflectivity (dBZ), (b) radial velocity (m s$^{-1}$), (c) spectrum width (m s$^{-1}$), and (d) correlation coefficient. The black semicircle is the 25-km radar range ring. (right) Radar variables from the 0.5° PPI scan from the Ku band of the D3R during OLYMPEX at 1454 UTC 17 Dec 2015: (e) reflectivity (dBZ), (f) radial velocity (m s$^{-1}$), (g) spectrum width (m s$^{-1}$), and (h) correlation coefficient. The black circles show the 5-, 15-, and 25-km radar range rings. The diagonal black line represents the Washington coast.
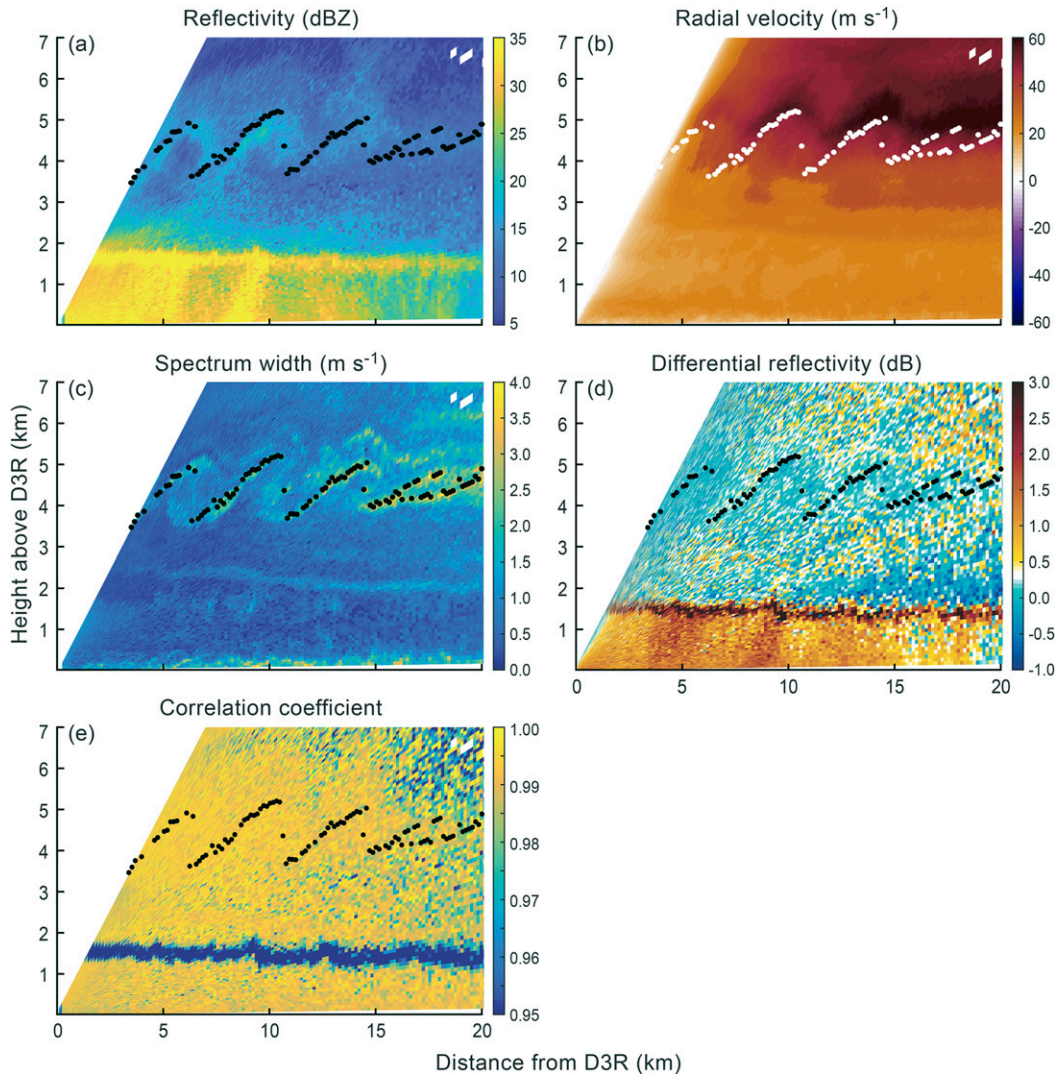
FIG. 9. Radar variables from an RHI scan from the Ku band of the D3R at an azimuthal angle of 56° at 0706 UTC 9 Dec 2015: (a) reflectivity (dB$Z$), (b) radial velocity (m s$^{-1}$), (c) spectrum width, (d) differential reflectivity (dB), and (e) correlation coefficient. The black dots in (a) and (c)–(e) and the white dots in (b) show the location of the maximum spectrum width in each vertical column.

enhanced $Z_{DR}$ located at an altitude of 1.5 km. These dual-polarization signatures are associated with melting particles (e.g., Zrnić et al. 1993; Straka et al. 2000; Brandes and Ikeda 2004; Andrić et al. 2013). While the highest $Z_H$ values are associated with the bright band, it is shown in Fig. 9a that $Z_H$ was being enhanced by approximately 5 dB$Z$ approximately 5–10 km away from the radar at altitudes between 3 and 5 km. Differential reflectivity appeared to have been slightly reduced immediately below the SW filaments. While both variables are subject to attenuation, this pattern of enhanced $Z_H$ and reduced $Z_{DR}$ provides insight into the microphysical processes induced by the KH waves.

The top of the KH perturbations reached approximately 5 km where the temperature was nearly −20°C (Fig. 4b), which is the coldest temperature allowing aggregation (e.g., Hobbs et al. 1974). Thus, the waves were perturbing particles warmer than −20°C and aggregation was likely to occur. Riming would have been unlikely because the environment above the KH waves is relatively dry (Fig. 4b). Therefore, the high $Z_H$ in the filaments indicates that the particles were larger as a result of aggregation, not water-coated or rimed hydrometeors. The lower $Z_{DR}$ below the filaments was likely the result of turbulent motions disorienting the aggregates and other platelike particles so that they were falling without a preferred orientation

(e.g., Bringi and Chandrasekar 2001). This inference is consistent with the absence of a reduction in $\rho_{HV}$ (Fig. 9e).

Below the bright band, the analysis presented in Figs. 9a and 9d shows that $Z_H$ and $Z_{DR}$, respectively, increased about 5 and 10 km away from the radar. This dual-polarization pattern indicates that larger raindrops were located in these regions (e.g., Straka et al. 2000; Kumjian and Ryzhkov 2012). While these regions of enhancement appear to have had the same period as the waves aloft, we cannot determine from the available data whether they were the result of the melting and fallout of wave-aggregated ice. We note, however, that $Z_H$ associated with the second filament from the left connects to the region of increased $Z_H$ above the bright band in Fig. 9a. The upward right-to-left tilt of this reflectivity filament resulted from the stronger vertical wind shear advecting hydrometeors aloft faster than hydrometeors near the surface.

### b. RHI scans when KH waves are within the melting layer

The DOW radar observed one of the most prominent KH wave events during OLYMPEX on 12 December 2015. A representative cross section at an azimuthal angle of 54° through these waves is shown in Fig. 10 at 2110 UTC. The format of Fig. 10c is the same as Fig. 9. The bright band, identified by its reduced $\rho_{HV}$, enhanced $Z_{DR}$, and enhanced $Z_H$, is seen in Fig. 10 to be approximately 0.5–1 km above the radar (e.g., Zrnić et al. 1993; Straka et al. 2000; Brandes and Ikeda 2004; Andrić et al. 2013). The black dots trace out the central access of the waves and demonstrate that the base of the KH waves coincided with the top of the bright band/melting layer.

The data presented in Fig. 10b indicate that winds aloft were away from the radar and that winds near the surface were toward the radar, which implies clockwise circulation in the plane of the cross section. One of the upward branches of these circulations was approximately 6 km away from the radar. While $Z_H$ data presented in Fig. 10a show that $Z_H$ was enhanced throughout the wave, two local maxima in reflectivity were observed approximately 6 and 11 km away from the radar at 1.5 km in altitude. These reflectivity maxima occurred within the upward branch of the waves and the reflectivity maxima located 11 km from the radar was clearly distinct from the bright band. The analysis presented in Fig. 10e indicates that the trough and a portion of the upward branch of the wave was characterized by reduced $\rho_{HV}$ up to nearly 1.5 km above the radar. Above 1.5 km the $\rho_{HV}$ perturbation disappeared. Figure 10d shows enhanced $Z_{DR}$ in the trough and upward branch up to 1.5 km—an enhancement observed despite potential differential attenuation remaining in these data. A similar pattern was observed 10 km away from the radar.

The dual-polarization perturbations associated with these waves likely resulted from a combination of wave-induced advection and wave-induced microphysical modification. The turbulent mixing induced by the waves likely accounted for some of the $\rho_{HV}$, $Z_{DR}$, and $Z_H$ perturbations, especially within the trough of waves (e.g., Zrnić et al. 1993; Zrnić and Ryzhkov 1999). However, the waves could have had a direct microphysical impact on the hydrometeors. Riming causes similar $\rho_{HV}$, $Z_{DR}$, and $Z_H$ perturbations, and it could have occurred when preexisting ice particles encountered supercooled water that was generated by the KH waves and/or advected liquid water vertically by the KH waves above the 0°C level (e.g., Aydin and Seliga 1984; Straka et al. 2000). Given that $\rho_{HV}$ abruptly increased above 1.5 km, it is likely that riming occurred only below 1.5 km. This idea is consistent with the local maximum in $Z_H$ occurring at 1.5 km. Aggregation causes an increase in $Z_H$ and a decrease in $Z_{DR}$ (Bader et al. 1987; Straka et al. 2000; Andrić et al. 2013), and turbulence associated with the KH wave could have also enhanced this process. While the dual-polarization signature of aggregation at low altitudes could have been masked by the stronger signature associated with riming, the arches of enhanced $Z_H$ above 1.5 km with relative enhancements in $Z_{DR}$ indicate that larger particles were present throughout the wave.

The 12 December 2015 case was similar to the Houser and Bluestein (2011) event, as both were located near a bright band, had similar dual-polarization perturbations, and suggested that KH waves induce riming. Both cases were characterized by enhanced $Z_H$ and $Z_{DR}$ and reduced $\rho_{HV}$ in the upward branch of the waves. The 12 December 2015 case differed from the Houser and Bluestein (2011) case in that enhanced $Z_H$ was observed throughout the wave and the regions of reduced $\rho_{HV}$ were more expansive. Additionally, SW in Fig. 10c was enhanced along the entire central axis of the wave, not only downwind of the crest of the waves as suggested by Houser and Bluestein (2011). Thus, our results suggest that the microphysical impact of KH waves is slightly larger than is suggested by Houser and Bluestein (2011). We expect that these differences exist because the data used by Houser and Bluestein (2011) had a coarser vertical resolution and could not resolve these finescale details.

### c. RHI scans when KH waves are below the melting layer

A layer of strong vertical wind shear between 0.5 and 1.5 km above the surface at 1320 UTC 17 December 2015 at azimuth 254° is seen in Figs. 11b and 11c. This shear fostered KH waves for several hours (Table 1). We chose this RHI because it provides evidence of the microphysical impact of the KH waves on warm-rain processes. The bright band was clearly identifiable between
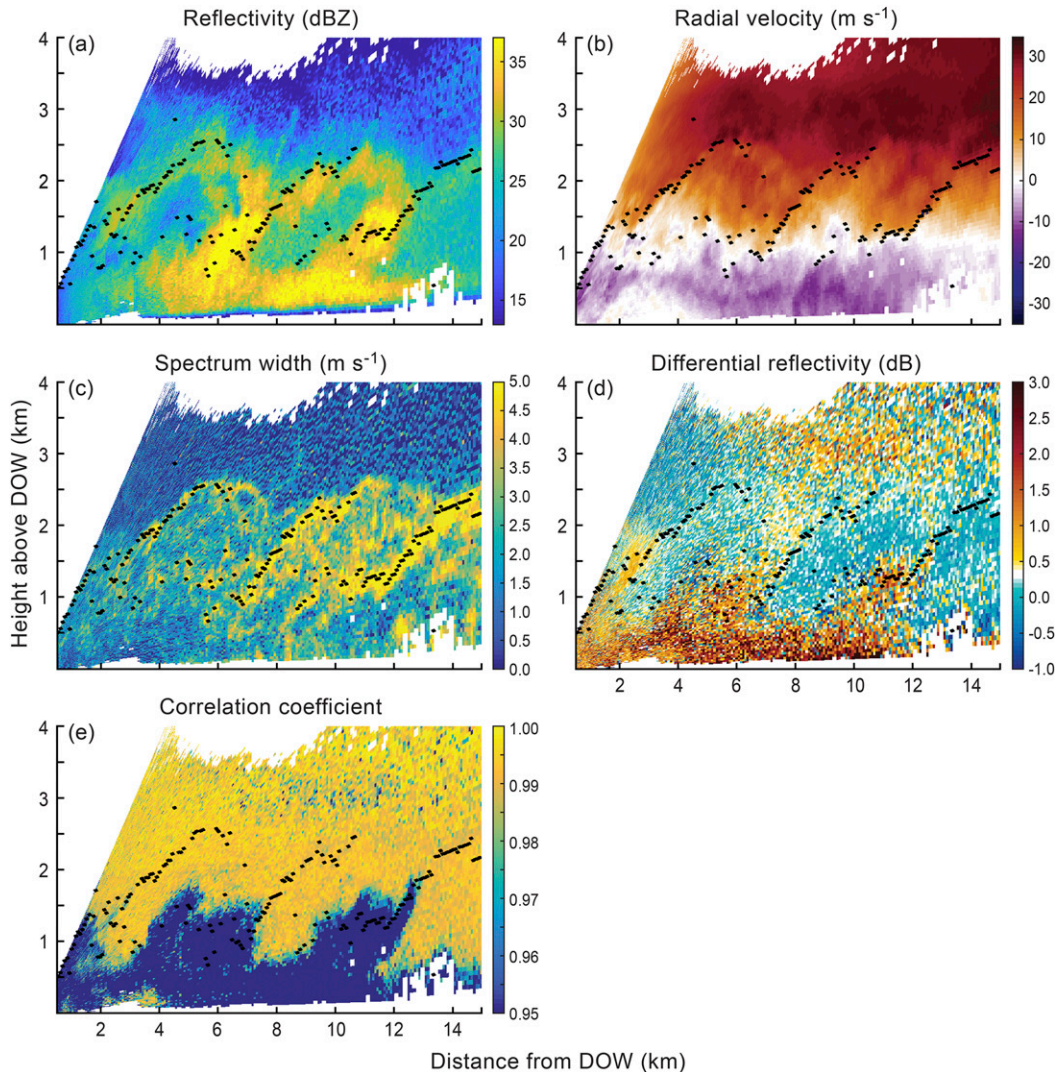
FIG. 10. As in Fig. 9, but for an RHI scan from the DOW radar at an azimuthal angle of 54° at 2110 UTC 12 Dec 2015. The black dots show the location of the maximum spectrum width in each vertical column.

altitudes 2 and 2.5 km in Figs. 11a, 11d, and 11e as enhanced $Z_H$, enhanced $Z_{DR}$, and reduced $\rho_{HV}$.

The SW cross section (Fig. 11c) indicates that the waves extended from the surface to ~1.5 km, which was well below the bright band. However, the analysis presented in Figs. 11d and 11e shows a slightly wavy pattern of $Z_{DR}$ and $\rho_{HV}$ within the bright band itself, especially within 5 km of the radar. Additionally, small pockets of enhanced $Z_H$ existed in the bright band just above and downstream of the wave crests (Fig. 11a). These waves in the bright band suggest that momentum transfer by the KH waves was being felt at relatively far distances from the layer containing the most active portions of the waves. This conclusion is further supported by the analysis presented in Fig. 11b, which shows that $V_R$ perturbations associated with the wave existed up to

3 km above the ground. Previous studies, including Luce et al. (2008), have also observed oscillations in regions that are relatively far from the KH waves.

Four waves, each characterized by slightly enhanced $Z_H$ within and beneath the upward branches of the central axis of the waves and slightly reduced $Z_H$ within their downward branches at altitudes below 1.5 km are shown in Fig. 11a. This oscillating pattern was also seen in the $Z_{DR}$ data (Fig. 11d). Regions of increased $Z_H$ and $Z_{DR}$ are associated with larger raindrops.

There are several microphysical processes that could account for an increase in the size of raindrops beneath the crest of the waves. First, the waviness in the bright band suggests that liquid water might have been fluxed above the freezing level and, as discussed in section 5b, fostered riming. Being larger and/or denser, such rimed
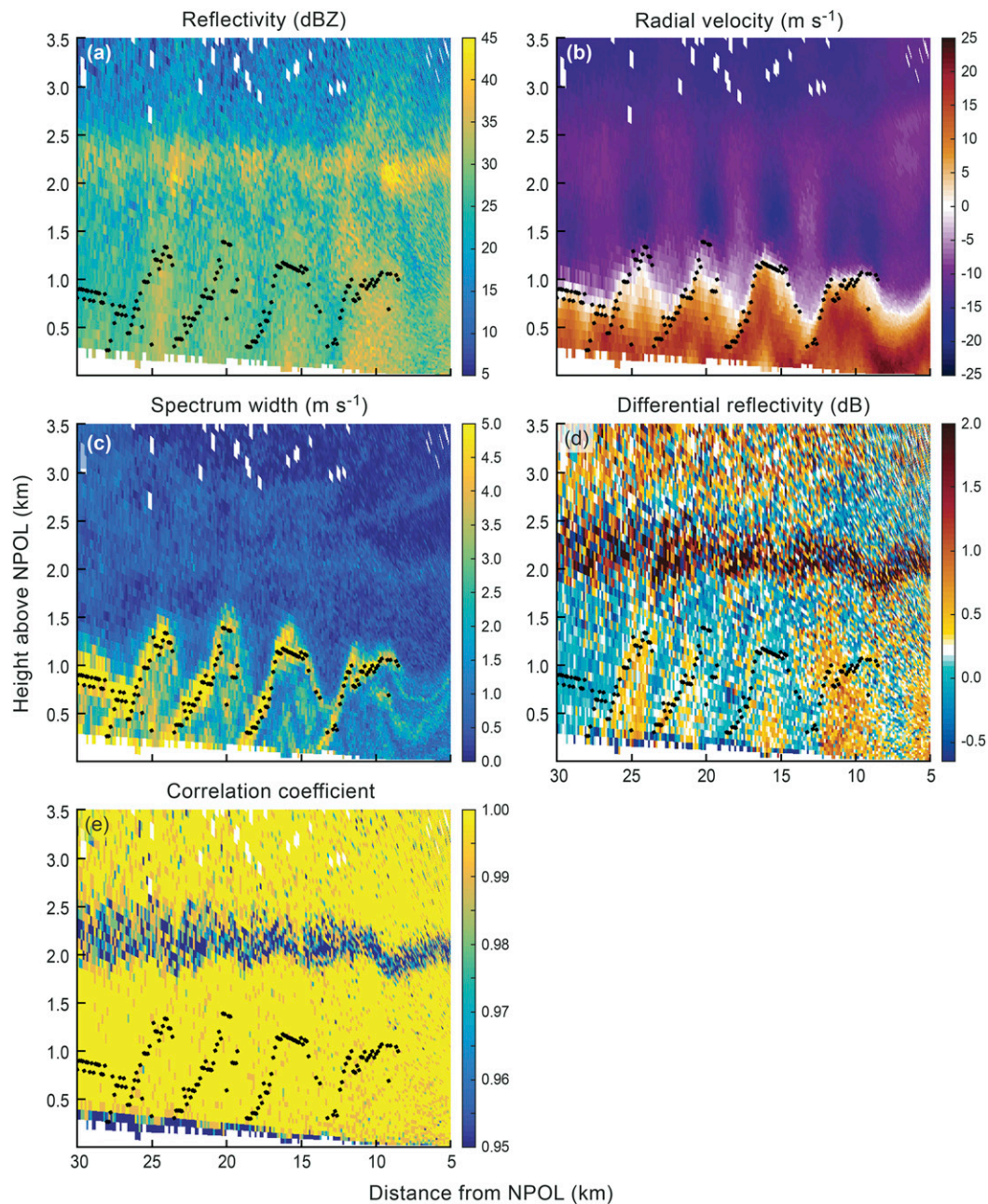
FIG. 11. As in Fig. 9, but for an RHI scan from the NPOL during OLYMPEX at an azimuthal angle of 254° at 1320 UTC 17 Dec 2015. The black dots show the location of the maximum spectrum width in each vertical column. Note that the x coordinate origin is on the right side of each panel. The x axis was flipped so that the orientation of the waves is consistent throughout the paper.

ice particles could create larger drops as they melted below the 0°C level. If the enhanced $Z_H$ below the waves was primarily attributable to the melting rimed particles, one would expect to see enhanced $Z_H$ extend continuously downward from the bright band. However, there was a $Z_H$ minimum just below the bright band. Thus, rimed particles were likely not the primary

cause of the perturbations observed below 1.5 km. The rawinsonde data presented in Fig. 4d indicate that the atmosphere was nearly saturated below 5 km. Thus, the wave-induced upward motion likely produced additional increased vapor deposition on the preexisting raindrops. Additionally, the analysis in Figs. 11a and 11d shows that $Z_H$ and $Z_{DR}$ were
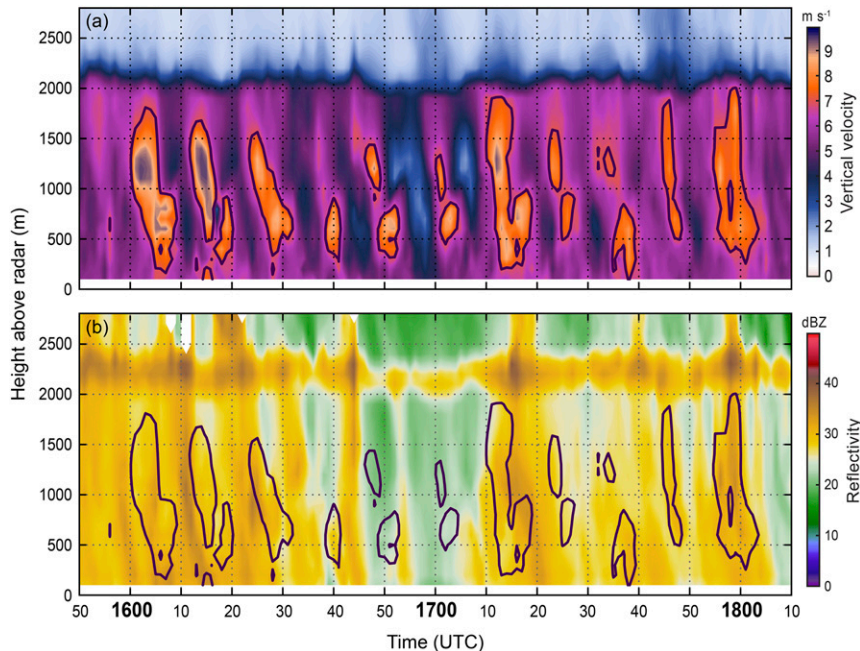
FIG. 12. Time series of the MRR data from 1550 to 1810 UTC 17 Dec 2015 of vertical profiles of (a) vertical fall velocity (shading; m s$^{-1}$) and (b) reflectivity (shading; dB$Z$). The black contours outline regions where downward vertical velocities are at least 7 m s$^{-1}$.

enhanced beneath the waves, which suggests that hydrometeors increased in size as they fell (e.g., Straka et al. 2000; Kumjian and Ryzhkov 2012). These large nearsurface particles could have been created by increased coalescence fostered by wave-induced turbulence (e.g., Kumjian and Prat 2014). Both vapor deposition and coalescence would have created larger drops (>2-mm diameter), especially coalescence. The modest upward motion associated with the KH waves would not keep such relatively large drops from falling, and their fallout would account for the increased $Z_H$ and $Z_{DR}$ below the central axis of the waves.

While the analysis presented in Fig. 11 clearly shows that the KH waves were associated with oscillations in the dual-polarization data, the magnitude of these oscillations in the radar data was small (e.g., ~10 dB in reflectivity). To investigate if these KH waves below the melting level modified, surface precipitation disdrometer and vertically pointing radar data are explored in the next section.

### d. Ground observations when KH waves are below melting layer

Ground observations on 17 December 2015 provide evidence that the KH waves below the melting level slightly modified the characteristics of the raindrops, although not enough to significantly change accumulated precipitation at the surface below the waves. To the authors' knowledge, this is the first time such KH oscillations have been documented in ground observations of

the particle drop size distribution. Several instruments, including an MMR and a PARSIVEL-2, were located at the Fishery site, 20 km northeast of NPOL. The $Z_H$ and vertical velocity data obtained between 1550 and 1810 UTC 17 December 2015 by the vertically pointing MRR are shown in Fig. 12. Downward vertical motion in excess of 7 m s$^{-1}$ is outlined by a black contour in both panels. A time series of the MRR particle mean fall speed and $Z_H$ at 500-m elevation are shown in Fig. 13a for the same period on 17 December 2015 as Fig. 12. An oscillating pattern is evident in the vertical velocity data. Close inspection of Figs. 12b and 13a reveals a slight enhancement in $Z_H$ (~5 dB$Z$) immediately following the peak downward vertical motion. This lag of several minutes between the enhanced $Z_H$ and the peak downward velocity suggests that larger drops formed within the upward branch of the waves and fell out shortly after the peak upward motion.

PARSIVEL-2 observations of rain rate for the same time period is shown in Fig. 13b and the mass-weighted mean drop diameter $D_m$ is shown in Fig. 13c. While there was a large amount of high-frequency variability, especially prior to 1610 UTC and after 1710 UTC, four coherent peaks in rain rate occurred between 1610 and 1700 UTC (at 1625, 1635, 1643, and 1653 UTC). Peaks in $D_m$ occurred at roughly the same times. The last two perturbations (at 1643 and 1653 UTC) are the most distinct, and a comparison with Fig. 13b indicates that they are collocated with the rain-rate peaks. The
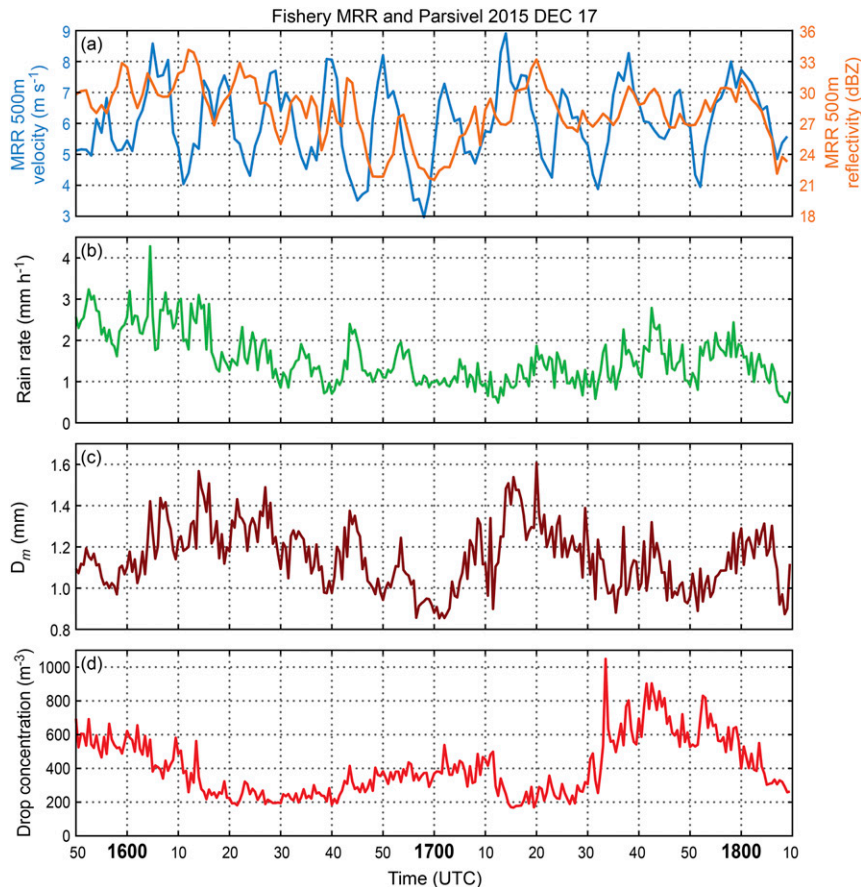
FIG. 13. Time series from 1550 to 1810 UTC 17 Dec 2015 of (a) 500-m vertical velocities (blue contour; m s$^{-1}$) and 500-m reflectivity (gold contour; dB$Z$), (b) surface rain rate (mm h$^{-1}$) in 30-s intervals, (c) mass-weighted mean droplet diameter (mm), and (d) droplet concentration (m$^{-1}$). Data are from (a) the MRR and (b)–(d) the PARSIVEL-2, both at the Fishery ground site.

largest drops $D_{max}$ observed in these four peaks were approximately 2.3–2.8 mm in diameter. This increase in $D_m$ is direct evidence that these waves are creating larger drops, possibly as a result of increased vapor deposition and/or turbulence-induced coalescence. However, the amplitude of these anomalies is small, less than 0.5 mm.

A comparison of Figs. 13a and 13b indicates that the rain rate is maximized 3–5 min after the fall speed maximum, consistent with Figs. 11 and 12. A power spectrum analysis of exactly 1 h of the PARSIVEL-2 rain-rate data between 1605 and 1705 UTC is shown in Fig. 14. The rain-rate anomaly (with the mean removed) in Fig. 14a appears to have five periodic spikes. The analysis presented in Fig. 14b shows that the spectral power is concentrated in the sixth harmonic, corresponding to a wave frequency of 6 h$^{-1}$. The portion of the rain-rate anomaly associated with the sixth harmonic is shown in Fig. 14c. The peaks of the periodic signal in Fig. 14c align with the peaks in Fig. 14a, indicating that the KH waves are responsible for the periodic signal. The power spectrum analysis indicates

that the waves at this time had a 10-min frequency and are responsible for a 0.3 mm h$^{-1}$ rain-rate perturbation, which is rather small considering the impressive velocity perturbations and supports our previous conclusion that the KH waves had only a minor microphysical impact on warm-rain processes on 17 December 2017. The analysis presented in Fig. 13d shows no coherent oscillations in droplet concentration on the time scale of the KH waves.

The data described here indicate that precipitation process variability had a variety of time scales during the event of 17 December 2015, with KH waves being just one component of the variability. From the NPOL, MRR, and PARSIVEL-2 data, it is apparent that upward motion within KH waves altered the microphysical processes by creating larger drops as a result of enhanced depositional growth and/or increased turbulence-induced coalescence. However, the amplitudes of the wave-induced perturbations are small, and the KH waves did not have a significant impact on accumulated precipitation or drop concentration.
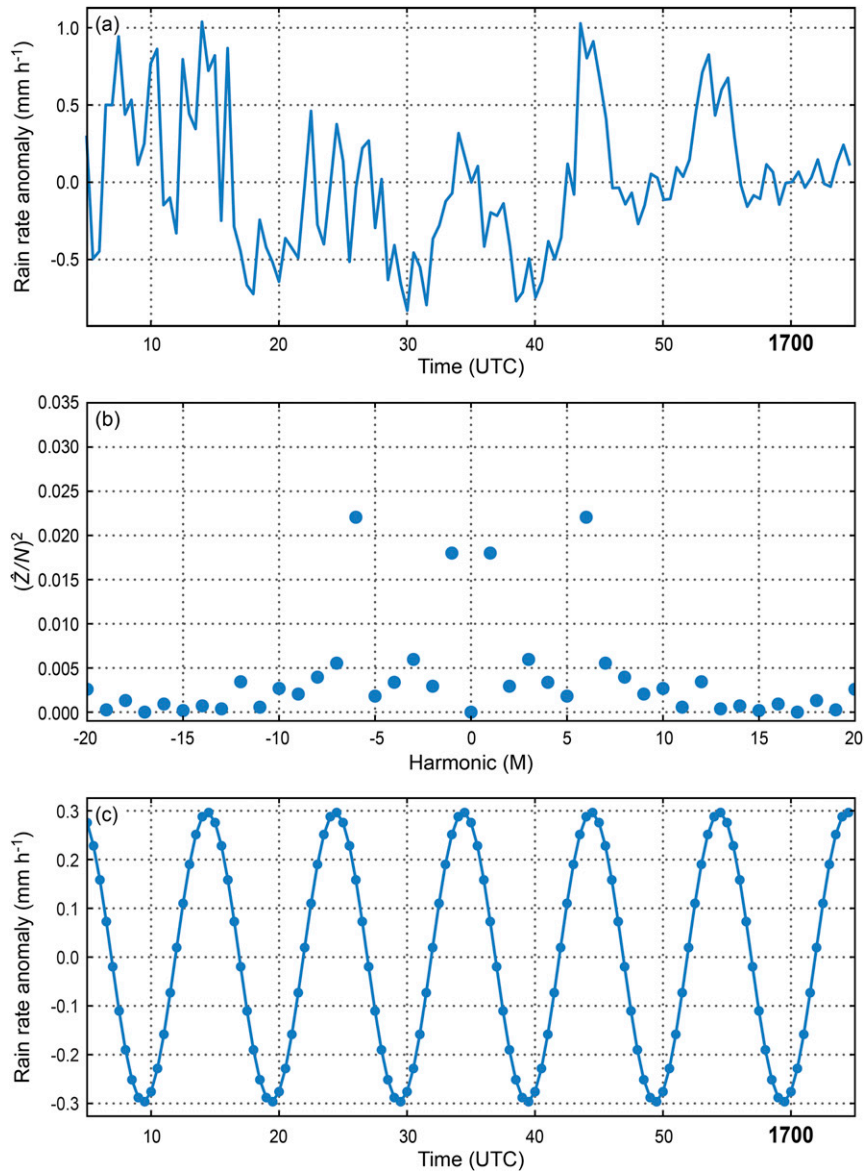
FIG. 14. Power spectrum analysis of the PARSIVEL-2 data from 1605 to 1705 UTC 17 Dec 2015: (a) time series of the rain rate with the mean removed, (b) periodogram of spectral power associated with the ±20 harmonics, and (c) rain-rate anomaly associated with the six harmonic (10-min frequency).

## 6. Impact of topography

An NPOL RHI over land at 1532 UTC 17 December 2015 (Fig. 15) reveals KH waves encountering the foothills of the Olympic Mountains. Figures 11 and 15 show data from RHI scans within 20 min of each other. However, the KH waves were located over the ocean in Fig. 11 and they are located over the foothills in Fig. 15. The black dots depict the central axis of the waves, and the white regions along the bottom of each panel show the topography of the mountains.

The data presented in Fig. 15 suggest that upward-sloping terrain can impact the amplitude of KH waves. Approximately 30 km away from NPOL the amplitude of the KH waves abruptly and rapidly increases (rapid jump in black dots). This amplitude jump coincides with the leading edge of the high terrain and may have occurred because the terrain increased the vertical wind shear, which would have decreased Ri and allowed the amplitude of the wave to increase (Houze and Medina 2005; Medina et al. 2005). Additionally, the terrain itself
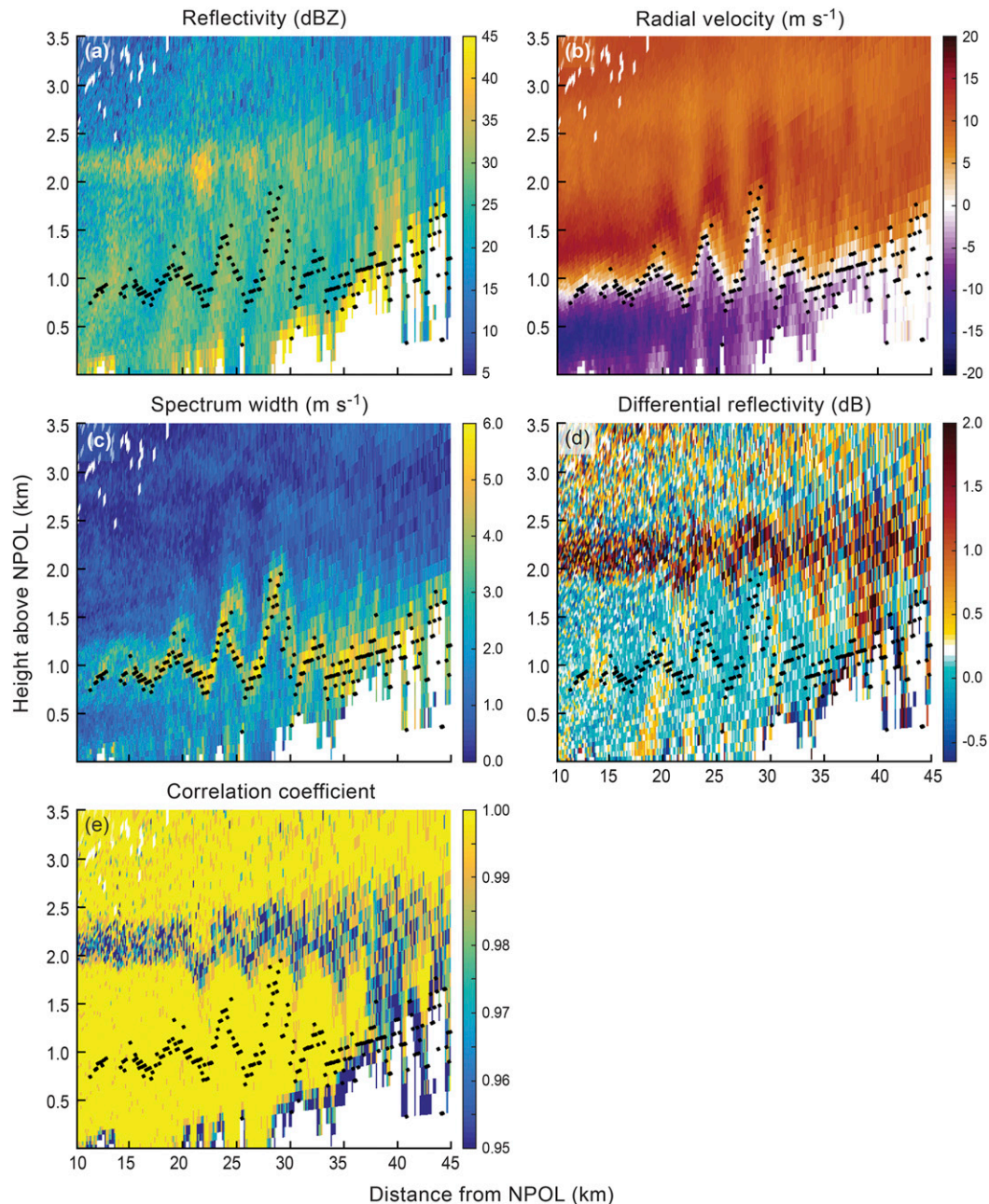
FIG. 15. As in Fig. 10, but for an RHI scan from the NPOL at an azimuthal angle of 54° at 1352 UTC 17 Dec 2015.

could have forced additional upward motion in the KH wave. Future studies will be necessary in order to determine the exact cause of this rapid increase in the wave amplitude along the leading edge of the terrain.

## 7. Conclusions

We have analyzed four KH wave events embedded within precipitating extratropical cyclones to assess the microphysical impact of KH waves on precipitation

processes and to investigate how mountains impact KH waves. By comparing one inland KH wave event over the Midwest (during IFloodS) with three KH wave events near the mountainous Washington coast (during OLYMPEX) this study demonstrates the following:

1) KH waves occur within the precipitating clouds of midlatitude cyclones regardless of the presence or absence of mountains. KH waves can occur at any altitude that has high static stability and strong vertical
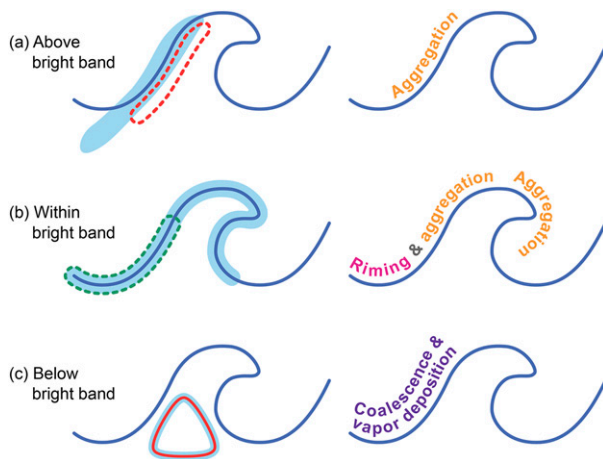
FIG. 16. Conceptual diagrams showing (left) how KH waves perturb dual-polarization variables and (right) the microphysical processes induced by them (a) above, (b) within, and (c) below the melting layer. In the left column, blue shading represents reflectivity perturbations, red represents differential reflectivity perturbations, and green represents correlation coefficient perturbations. Solid lines depict positive perturbations. Dashed lines depict negative perturbations.

wind shear. These results are consistent with previous studies (e.g., Chapman and Browning 1997; Wakimoto et al. 1992; Friedrich et al. 2008; Houser and Bluestein 2011; Medina and Houze 2015, 2016).

2) KH waves can modify both the liquid- and ice-phase microphysics as revealed in dual-polarization radar variables. While KH waves have a microphysical impact on hydrometeors at all altitudes, their effects vary depending on the position of the KH waves relative to the melting level (Fig. 16).

3) Dual-polarization radar variables suggests that turbulence associated with the KH waves enhances aggregation in the upward branch of the KH wave everywhere above the bright band and enhances riming near the bright band.

4) OLYMPEX documented one case in which KH waves occurred below the bright band and produced oscillatory behavior in the particle fall velocity, surface rain rate, and mass-weighted mean drop diameter. Dual-polarization radar variables indicate that these changes to the hydrometeor characteristics are related to enhanced coalescence and/or vapor deposition within the upward branch of KH waves. To the authors' knowledge this is the first time oscillatory behavior associated with KH waves has been documented in ground observations of the particle size distribution.

5) Complex terrain can make conditions more favorable to KH wave development by increasing shear and stability within baroclinic zones approaching a mountain range. Upward-sloping terrain may also impact the structure of the KH waves by increasing their amplitude.

These results advance our understanding of the microphysical impact of KH waves by analyzing high-resolution vertical data that capture smaller-scale features of the KH waves and by exploring cases where KH waves occur above and below the melting level. As summarized in Fig. 16, when located above the bright band, the upward branch of KH waves are characterized by slight increases in $Z_H$ and decreases in $Z_{DR}$, indicating that the waves contain aggregates that are randomly oriented within the turbulent air motions. Waves within the bright band are also characterized by enhanced $Z_H$, implying larger particles that are either rimed or randomly oriented melting aggregates. The reduced $\rho_{HV}$ in the suggests that the upward branch of waves within the bright band could support riming by transporting liquid water above the melting level or through the local generation of supercooled liquid water in the saturated air. These results are consistent with Houze and Medina (2005) and Houser and Bluestein (2011) in terms of the possible microphysical impact of KH waves near the melting level in midlatitude precipitating systems. In the case where the waves are located below the melting level, enhanced $Z_H$ and $Z_{DR}$ observed below the upward portions of the waves indicate the fallout of large water drops that likely resulted from increased vapor deposition or coalescence in the upward branch.

A significant question is whether KH waves impact surface precipitation accumulations. This study is uniquely able to explore this question because the KH waves observed during the 17 December 2015 OLYMPEX event occurred over several ground instruments, including an MRR and a PARSIVEL-2 disdrometer. To the authors' knowledge this is the first study to clearly document the presence of KH waves in ground observations. While oscillations in drop size and rain rate were observed at the surface, the KH waves appeared to enhance precipitation accumulations only slightly. KH waves centered in shear layers at or above the melting level could produce effects on downstream snow accumulation over the higher terrain (e.g., Houze and Medina 2005), but the data available to this study do not easily allow for this possibility to be explored.

Additionally, the question remains as to how the mountainous topography impacts the formation and structure of KH waves. Previous studies hypothesized that the upward-sloping terrain of a mountain range can modify atmospheric conditions so that they are more favorable to KH wave development by enhancing shear and stability layers associated with frontal boundaries (Medina and Houze 2015; Medina et al. 2005). Results from this study seem to support this theory. KH waves were observed relatively frequently during OLYMPEX

under moderately (i.e., not strongly) stable large-scale conditions, including at least a half dozen additional instances not detailed in this manuscript. KH waves during some of these OLYMPEX events were observed for several hours. On the other hand, the KH waves during IFloodS were observed briefly within an anomalously strong stationary front (Fig. 4), similar to large-scale conditions associated with the KH waves in the Houser and Bluestein (2011) Oklahoma study. The OLYMPEX data also indicated that the amplitude of the waves and possibly the strength of their associated microphysical effects can rapidly increase near the forward slopes of the terrain. Additional observational studies and numerical simulations (e.g., Conrick et al. 2018) are required to directly address the role topography plays on KH wave frequency, amplitude, time evolution, and impact.

REFERENCES

Andrić, J., M. R. Kumjian, D. S. Zrnić, J. M. Straka, and V. M. Melnikov, 2013: Polarimetric signatures above the melting layer in winter storms: An observational and model study. *J. Appl. Meteor. Climatol.*, **52**, 682–700, https://doi.org/10.1175/JAMC-D-12-028.1.

Atlas, D., J. I. Metcalf, J. H. Richter, and E. E. Gossard, 1970: The birth of "CAT" and microscale turbulence. *J. Atmos. Sci.*, **27**, 903–913, https://doi.org/10.1175/1520-0469(1970)027<0903:TBOAMT>2.0.CO;2.

Aydin, K., and T. A. Seliga, 1984: Radar polarimetric backscattering properties of conical graupel. *J. Atmos. Sci.*, **41**, 1887–1892, https://doi.org/10.1175/1520-0469(1984)041<1887:RPBPOC>2.0.CO;2.

Bader, M. J., S. A. Clough, and G. P. Cox, 1987: Aircraft and dual-polarization radar observations of hydrometeors in light stratiform precipitation. *Quart. J. Roy. Meteor. Soc.*, **113**, 491–515, https://doi.org/10.1002/qj.49711347605.

Brandes, E. A., and K. Ikeda, 2004: Freezing-level estimation with polarimetric radar. *J. Appl. Meteor.*, **43**, 1541–1553, https://doi.org/10.1175/JAM2155.1.

Bringi, V. N., and V. Chandrasekar, 2001: *Polarimetric Doppler Weather Radar.* Cambridge University Press, 636 pp.

Browning, K. A., 1971: Structure of the atmosphere in the vicinity of large-amplitude Kelvin-Helmholtz billows. *Quart. J. Roy. Meteor. Soc.*, **97**, 283–299, https://doi.org/10.1002/qj.49709741304.

——, and C. D. Watkins, 1970: Observations of clear air turbulence by high power radar. *Nature*, **227**, 260–263, https://doi.org/10.1038/227260a0.

——, J. H. Marsham, B. A. White, and J. C. Nicol, 2012: A case study of a large patch of billows surmounted by elevated convection. *Quart. J. Roy. Meteor. Soc.*, **138**, 1764–1773, https://doi.org/10.1002/qj.1908.

Chapman, D., and K. A. Browning, 1997: Radar observations of wind-shear splitting within evolving atmospheric Kelvin-Helmholtz billows. *Quart. J. Roy. Meteor. Soc.*, **123**, 1433–1439, https://doi.org/10.1002/qj.49712354114.

Conrick, R. J., C. F. Mass, and Q. Zhong, 2018: Simulated Kelvin–Helmholtz waves over terrain and their microphysical implications. *J. Atmos. Sci.*, https://doi.org/10.1175/JAS-D-18-0073.1, in press.

Dutton, J., and H. A. Panofsky, 1970: Clear air turbulence: A mystery may be unfolding. *Science*, **167**, 937–944, https://doi.org/10.1126/science.167.3920.937.

Friedrich, K., D. E. Kingsmill, C. Flamant, H. V. Murphy, and R. M. Wakimoto, 2008: Kinematic and moisture characteristics of a non-precipitating cold front observed during IHOP. Part II: Alongfront structures. *Mon. Wea. Rev.*, **136**, 3796–3797, https://doi.org/10.1175/2008MWR2360.1.

Geerts, B., and Q. Miao, 2010: Vertically pointing airborne Doppler radar observations of Kelvin–Helmholtz billows. *Mon. Wea. Rev.*, **138**, 982–986, https://doi.org/10.1175/2009MWR3212.1.

Gossard, E. E., J. H. Richter, and D. Atlas, 1970: Internal waves in the atmosphere from high-resolution radar measurements. *J. Geophys. Res.*, **75**, 3523–3536, https://doi.org/10.1029/JC075i018p03523.

Hallett, J., and S. C. Mossop, 1974: Production of secondary ice particles during the riming process. *Nature*, **249**, 26–28, https://doi.org/10.1038/249026a0.

Hobbs, P. V., S. Chang, and J. D. Locatelli, 1974: The dimensions and aggregation of ice crystals in natural cloud. *J. Geophys. Res.*, **79**, 2199–2206, https://doi.org/10.1029/JC079i015p02199.

Hou, A. Y., and Coauthors, 2014: The Global Precipitation Measurement Mission. *Bull. Amer. Meteor. Soc.*, **95**, 701–722, https://doi.org/10.1175/BAMS-D-13-00164.1.

Houser, J. L., and H. B. Bluestein, 2011: Polarimetric Doppler radar observations of Kelvin–Helmholtz waves in a winter storm. *J. Atmos. Sci.*, **68**, 1676–1702, https://doi.org/10.1175/2011JAS3566.1.

Houze, R. A., Jr., and S. Medina, 2005: Turbulence as a mechanism for orographic precipitation enhancement. *J. Atmos. Sci.*, **62**, 3599–3623, https://doi.org/10.1175/JAS3555.1.

——, and Coauthors, 2017: The Olympic Mountains Experiment (OLYMPEX). *Bull. Amer. Meteor. Soc.*, **98**, 2167–2188, https://doi.org/10.1175/BAMS-D-16-0182.1.

Kumjian, M. R., and A. V. Ryzhkov, 2012: The impact of size sorting on polarimetric radar variables. *J. Atmos. Sci.*, **69**, 2042–2060, https://doi.org/10.1175/JAS-D-11-0125.1.

——, and O. P. Prat, 2014: The impact of raindrop collision processes on polarimetric radar variables. *J. Atmos. Sci.*, **71**, 3052–3067, https://doi.org/10.1175/JAS-D-13-0357.1.

Luce, H., G. Hassenpflug, M. Yamamoto, S. Fukao, and K. Sato, 2008: High-resolution observations with MU radar of a KH instability triggered by an inertia–gravity wave in the upper part of a jet stream. *J. Atmos. Sci.*, **65**, 1711–1718, https://doi.org/10.1175/2007JAS2346.1.

Medina, S., and R. A. Houze Jr., 2015: Small-scale precipitation elements in midlatitude cyclones crossing the California Sierra Nevada. *Mon. Wea. Rev.*, **143**, 2842–2870, https://doi.org/10.1175/MWR-D-14-00124.1.

——, and ——, 2016: Kelvin-Helmholtz waves in extratropical cyclones passing over mountain ranges. *Quart. J. Roy. Meteor. Soc.*, **142**, 1311–1319, https://doi.org/10.1002/qj.2734.

——, B. F. Smull, R. A. Houze Jr., and M. Steiner, 2005: Cross-barrier flow during orographic precipitation events: Results from MAP and IMPROVE. *J. Atmos. Sci.*, **62**, 3580–3598, https://doi.org/10.1175/JAS3554.1.

——, E. Sukovich, and R. A. Houze Jr., 2007: Vertical structures of precipitation in cyclones crossing the Oregon Cascades. *Mon. Wea. Rev.*, **135**, 3565–3586, https://doi.org/10.1175/MWR3470.1.

Mesinger, F., and Coauthors, 2006: North American Regional Reanalysis. *Bull. Amer. Meteor. Soc.*, **87**, 343–360, https://doi.org/10.1175/BAMS-87-3-343.

Miles, J. W., and L. N. Howard, 1964: Note on a heterogeneous shear flow. *J. Fluid Mech.*, **20**, 331–336, https://doi.org/10.1017/S0022112064001252.

Newell, R. E., N. E. Newell, Y. Zhu, and C. Scott, 1992: Tropospheric rivers?—A pilot study. *Geophys. Res. Lett.*, **19**, 2401–2404, https://doi.org/10.1029/92GL02916.

NOAA/OAR/ESRL PSD, 2004: North American Regional Reanalysis data. NOAA/OAR/ESRL/PSD, accessed 24 August 2016, https://www.esrl.noaa.gov/psd/data/gridded/data.narr.html.

Petersen, W., and W. F. Krajewski, 2018: GPM Ground Validation Iowa FLood Studies (IFloodS) field campaign data collection. NASA EOSDIS Global Hydrology Resource Center Distributed Active Archive Center, accessed 14 March 2014, https://doi.org/10.5067/GPMGV/IFLOODS/DATA101.

——, and Coauthors, 2017: Olympic Mountain Experiment (OLYMPEX) for GPM ground validation collection. NASA Global Hydrology Resource Center Distributed Active Archive Center, accessed 28 July 2016, https://ghrc.nsstc.nasa.gov/home/content/olympex-datasets-currently-release.

Petre, J. M., and J. Verlinde, 2004: Cloud radar observations of Kelvin–Helmholtz instability in a Florida anvil. *Mon. Wea. Rev.*, **132**, 2520–2523, https://doi.org/10.1175/1520-0493(2004)132<2520:CROOKI>2.0.CO;2.

Pobanz, B. M., J. D. Marwitz, and M. K. Politovich, 1994: Conditions associated with large-drop regions. *J. Appl. Meteor.*, **33**, 1366–1372, https://doi.org/10.1175/1520-0450(1994)033<1366:CAWLDR>2.0.CO;2.

Ralph, F. M., P. J. Neiman, and G. A. Wick, 2004: Satellite and CALJET aircraft observations of atmospheric rivers over the Eastern North Pacific Ocean during the winter of 1997/98. *Mon. Wea. Rev.*, **132**, 1721–1745, https://doi.org/10.1175/1520-0493(2004)132<1721:SACAOO>2.0.CO;2.

Shapiro, M. A., 1980: Turbulent mixing within tropopause folds as a mechanism for the exchange of chemical constituents between the stratosphere and the troposphere. *J. Atmos. Sci.*, **37**, 994–1004, https://doi.org/10.1175/1520-0469(1980)037<0994:TMWTFA>2.0.CO;2.

Simpson, J. E., 1969: A comparison between laboratory and atmospheric density currents. *Quart. J. Roy. Meteor. Soc.*, **95**, 758–765, https://doi.org/10.1002/qj.49709540609.

Skofronick-Jackson, G., and Coauthors, 2017: The Global Precipitation Measurement (GPM) Mission for science and society. *Bull. Amer. Meteor. Soc.*, **98**, 1679–1695, https://doi.org/10.1175/BAMS-D-15-00306.1.

Straka, J. M., D. S. Zrnić, and A. V. Ryzhkov, 2000: Bulk hydrometeor classification and quantification using polarimetric radar data: Synthesis of relations. *J. Appl. Meteor.*, **39**, 1341–1372, https://doi.org/10.1175/1520-0450(2000)039<1341:BHCAQU>2.0.CO;2.

University of Wyoming, 2013: Davenport Iowa observations at 12Z 02 May. University of Wyoming, accessed 10 August 2017, http://weather.uwyo.edu/cgi-bin/sounding?region=naconf&TYPE=TEXT%3ALIST&YEAR=2013&MONTH=05&FROM=0212&TO=0212&STNM=74455.

Wakimoto, R. M., W. Blier, and C. Liu, 1992: The frontal structures of an explosive oceanic cyclone: Airborne radar observation of ERICA IOP 4. *Mon. Wea. Rev.*, **120**, 1135–1155, https://doi.org/10.1175/1520-0493(1992)120<1135:TFSOAE>2.0.CO;2.

Warner, M. D., C. F. Mass, and E. P. Salathé, 2012: Wintertime extreme precipitation events along the Pacific Northwest coast: Climatology and synoptic evolution. *Mon. Wea. Rev.*, **140**, 2021–2043, https://doi.org/10.1175/MWR-D-11-00197.1.

Weckwerth, T. M., and R. M. Wakimoto, 1992: The initiation and organization of convective cells atop a cold-air outflow boundary. *Mon. Wea. Rev.*, **120**, 2169–2187, https://doi.org/10.1175/1520-0493(1992)120<2169:TIAOOC>2.0.CO;2.

Zhu, Y., and R. E. Newell, 1994: Atmospheric rivers and bombs. *Geophys. Res. Lett.*, **21**, 1999–2002, https://doi.org/10.1029/94GL01710.

——, and ——, 1998: A proposed algorithm for moisture fluxes from atmospheric rivers. *Mon. Wea. Rev.*, **126**, 725–735, https://doi.org/10.1175/1520-0493(1998)126<0725:APAFMF>2.0.CO;2.

Zrnić, D. S., and A. V. Ryzhkov, 1999: Polarimetry for weather surveillance radars. *Bull. Amer. Meteor. Soc.*, **80**, 389–406, https://doi.org/10.1175/1520-0477(1999)080<0389:PFWSR>2.0.CO;2.

——, N. Balakrishnan, C. L. Ziegler, V. N. Bringi, and K. Aydin, 1993: Polarimetric signatures in the stratiform region of a mesoscale convective system. *J. Appl. Meteor.*, **32**, 678–693, https://doi.org/10.1175/1520-0450(1993)032<0678:PSITSR>2.0.CO;2.